Mesovortices within the 8 May 2009 Bow Echo over the Central United States: Analyses of the Characteristics and Evolution Based on Doppler Radar Observations and a High-Resolution Model Simulation

XIN XU

Key Laboratory of Mesoscale Severe Weather/Ministry of Education and School of Atmospheric Sciences, Nanjing University, Nanjing, China, and Center for Analysis and Prediction of Storms, University of Oklahoma, Norman, Oklahoma

MING XUE

Key Laboratory of Mesoscale Severe Weather/Ministry of Education and School of Atmospheric Sciences, Nanjing University, Nanjing, China, and Center for Analysis and Prediction of Storms and School of Meteorology, University of Oklahoma, Norman, Oklahoma

YUAN WANG

Key Laboratory of Mesoscale Severe Weather/Ministry of Education and School of Atmospheric Sciences, Nanjing University, Nanjing, China

(Manuscript received 16 July 2014, in final form 24 February 2015)

ABSTRACT

A derecho-producing bow-echo event over the central United States on 8 May 2009 is analyzed based on radar observations and a successful real-data WRF simulation at 0.8-km grid spacing. Emphasis is placed on documenting the existence, evolution, and characteristics of low-level mesovortices (MVs) that form along the leading edge of the bowing system. The genesis of near-surface high winds within the system is also investigated.

Significant MVs are detected from the radar radial velocity using a linear least squares derivatives (LLSD) method, and from the model simulation based on calculated vorticity. Both the observed and simulated bow-echo MVs predominantly form north of the bow apex. MVs that develop on the southern bow tend to be weaker and shorter-lived than their northern counterparts. Vortex mergers occur between MVs during their forward movement, which causes redevelopment of some MVs in the decaying stage of the bow echo. MVs located at (or near) the bow apex are found to persist for a notably longer lifetime than the other MVs. Moreover, the model results show that these bow-apex MVs are accompanied with damaging straight-line winds near the surface. These high winds are mainly caused by the descent of the rear-inflow jet at the bow apex, but the MV-induced vortical flow also has a considerable contribution. The locally enhanced descent of the rear-inflow jet near the mesovortex is forced primarily by the dynamically induced downward vertical pressure gradient force while the buoyancy force only plays a minor role there.

1. Introduction

Low-level, meso-γ-scale [2–20 km; Orlanski (1975)] mesovortices (MVs) are frequently observed at the leading edge of quasi-linear convective systems (QLCSs) like squall lines and bow echoes (e.g., Funk et al. 1999; Atkins et al. 2004). Recently, MVs have received increasing attention, owing to their propensity to produce damaging straight-line winds [i.e., derechoes; Johns and Hirt (1987)] near the surface (Weisman and Trapp 2003; Atkins et al. 2004; Wakimoto et al. 2006a; Wheatley et al. 2006; Atkins and St. Laurent 2009a,b). Moreover, bow-echo MVs have been observed to spawn tornadoes (Forbes and Wakimoto 1983; Przybylinski 1995).

The production of damaging winds within QLCSs has long been linked to the descent to the surface of a rear-inflow jet (RIJ) at the bow apex (Fujita 1978, 1979). Various factors have been implicated in the development

Corresponding author address: Ming Xue, School of Atmospheric Sciences, Nanjing University, Nanjing 210093, China.
E-mail: mxue@ou.edu

DOI: 10.1175/MWR-D-14-00234.1

of RIJs, such as the hydrostatically induced midlevel pressure minimum behind the leading convective updrafts (Lafore and Moncrieff 1989), horizontal buoyancy gradients related to the upshear-tilting convective circulation (Weisman 1992, 1993), and bookend (or line-end) vortices (Skamarock et al. 1994; Weisman and Davis 1998; Grim et al. 2009; Meng et al. 2012). Additionally, the RIJ strength had been found to be sensitive to ice microphysical processes as well as the environmental humidity (Yang and Houze 1995; Mahoney and Lackmann 2011).

However, the strongest straight-line wind damage may not be directly associated with the RIJ itself, but with low-level MVs along the bow echo, sometimes away from the bow apex. This was true in a severe bow echo that occurred near Saint Louis, Missouri, on 10 June 2003. This case was observed by the Bow Echo and Mesoscale Convective Vortex (MCV) Experiment (BAMEX; Davis et al. 2004) and detailed radar analyses and damage surveys performed by Atkins et al. (2005) revealed the strongest winds were associated with MVs. The important role of bow-echo MVs in determining the locations of intense straight-line wind damage was also documented by Wakimoto et al. (2006b) based on airborne Doppler radar analysis of a bow echo observed near Omaha, Nebraska, on 5 July 2003 (also a BAMEX case). More observational evidence was provided by Wheatley et al. (2006) through the investigation of five bow-echo events during BAMEX; it was found that most significant wind damage was typically associated with MVs in the bow-echo systems.

In light of their damage potential, MVs within QLCSs have also been studied through high-resolution numerical simulations. Low-level MVs were found to originate from downward or upward tilting of baroclinic horizontal vorticity generated along the cold outflow boundary and in general intensify as a result of vertical stretching (Trapp and Weisman 2003; Atkins and St. Laurent 2009b). The impact of ambient wind shear on MV structure and strength was assessed by Weisman and Trapp (2003) and Atkins and St. Laurent (2009a) through a series of idealized numerical simulations. Moderate-to-strong vertical wind shear at low to midlevels was found conductive to the formation of strong, deep, and long-lived MVs. Conversely, MVs were weak, shallow, and short lived in the case of weak wind shear. Moreover, the Coriolis force and strong cold pools were also found favorable for the genesis of strong MVs (Atkins and St. Laurent 2009a). Using real-data simulations, the effect of mesoscale heterogeneity on the genesis and structure of MVs was investigated by Wheatley and Trapp (2008). The simulated MVs were found to have developed as a consequence of mechanisms internal to the system, rather than due to interactions with external heterogeneities. However, the strength of the MVs was significantly affected by the meso-γ-scale heterogeneity in the form of a convective outflow boundary in their case.

A derecho-producing MCS with a large bow echo at its later stage occurred over the central United States on 8 May 2009 during the NOAA Hazardous Weather Testbed (HWT) 2009 Spring Experiment and was captured quite well by the Center for Analysis and Prediction of Storms (CAPS) real-time storm-scale ensemble forecasts (Xue et al. 2009; Kong et al. 2009). Coniglio et al. (2011) studied the environment conditions for the early evolution of the MCS on that day, and Coniglio et al. (2012) discussed the application of the Rotunno–Klemp–Weisman (RKW) theory (Rotunno et al. 1988) to this system. Their results showed that the initial storms of the MCS were initiated in an environment of weak synoptic-scale forcing and limited thermodynamic instability, with its structure and strength controlled by many factors. In the post-MCS stage, however, the system evolved in an environment of large thermodynamic instability, as will be shown in section 3a. The cold pool-ambient wind shear balance below 3 km was found not as important as the RKW theory suggested. Wind shear above 3 km appeared to be more critical for the case. Using a simulation with a 3-km grid spacing, Weisman et al. (2013) presented an analysis of the 8 May 2009 MCS, emphasizing the evolution of its thermodynamic and kinematic features (e.g., the warm-core meso-β-scale vortex or MCV that developed at the northern end of the system). Based on the same numerical simulation, Evans et al. (2014) examined the dynamical processes that contributed to the formation of the MCV, utilizing both quasi-Lagrangian circulation budget and backward trajectory analyses. While Evans et al. (2014) focused on the genesis of the line-end meso-β-scale vortex, many meso-γ-scale vortices did occur along the leading convective line of the system (Przybylinski et al. 2010). Lese and Martinaitis (2010) discussed two pairs of counter-rotating MVs detected by single-Doppler radar observations in this case. The formation mechanisms of the MVs in this case and in general are, however, still not well understood.

In this paper, we focus on the mature stage of the MCS of the 8 May 2009 over the central United States, in particular between 1200 and 1500 UTC when the MCS evolved into a well-defined bow echo. Numerous reports of high winds were produced by the bowing system, along with tens of tornadoes (Fig. 1) according to the Storm Prediction Center (SPC) reports (available online at http://www.spc.noaa.gov/climo/reports/090508_rpts.html.)

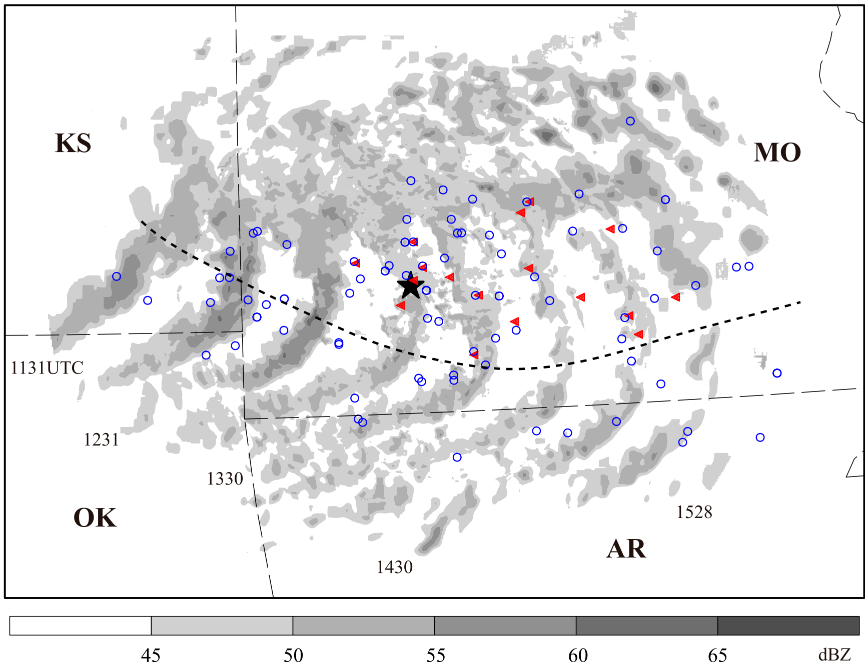

FIG. 1. Half-hourly reflectivity composite from the WSR-88D at Springfield, Missouri (KSGF, filled black star), high wind (>33.5 m s^{-1}, open blue circles), and tornado (filled red triangles) reports associated with the 8 May 2009 central U.S. bow-echo event from 1131 to 1528 UTC. The severe weather reports are from the Storm Prediction Center (SPC). The thick dashed line represents the approximate locus of the bow apex.

The emphasis of this study is on documenting the existence of low-level MVs in this bow-echo system and examining their general characteristics (e.g., lifetime and intensity) based on radar observations and a real-data numerical simulation. The results presented herein are one of the first of such a kind, where a high-resolution real data simulation of a bow-echo systems and embedded MVs are realistic enough to be directly comparable with radar measurements (e.g., Schenkman et al. 2011). The genesis of near-surface high winds within the bow echo is also investigated. A detailed dynamical analysis on the genesis mechanisms of the MVs in this case will be reported in a separate paper (Xu et al. 2015). An important goal of this paper is to establish the physical credibility of the model simulation of the MCS and in particular the model depiction of the MVs so as to lay a foundation for the detailed dynamical analysis in Xu et al. (2015).

The rest of this paper is organized as follows. Section 2 presents the data, method, and the setup of a numerical simulation. Section 3 describes the environmental conditions and gives an overview of the structure and evolution of the large bowing system. The MVs generated in the bow echo are identified and discussed based on radar observations and the numerical simulation in sections 4 and 5, respectively. Section 6 analyzes the generation of high winds within the simulated bowing system. A summary and further discussion are given in section 7.

2. Data, methodology, and experiment setup

Observations from the operational WSR-88D at Springfield, Missouri (KSGF), are used to help identify

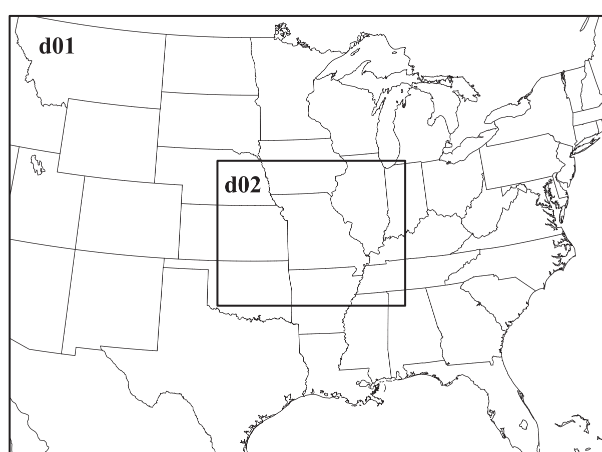

FIG. 2. Schematic of two-way interactive WRF Model domains used in this study with grid spacings of 4 and 0.8 km.

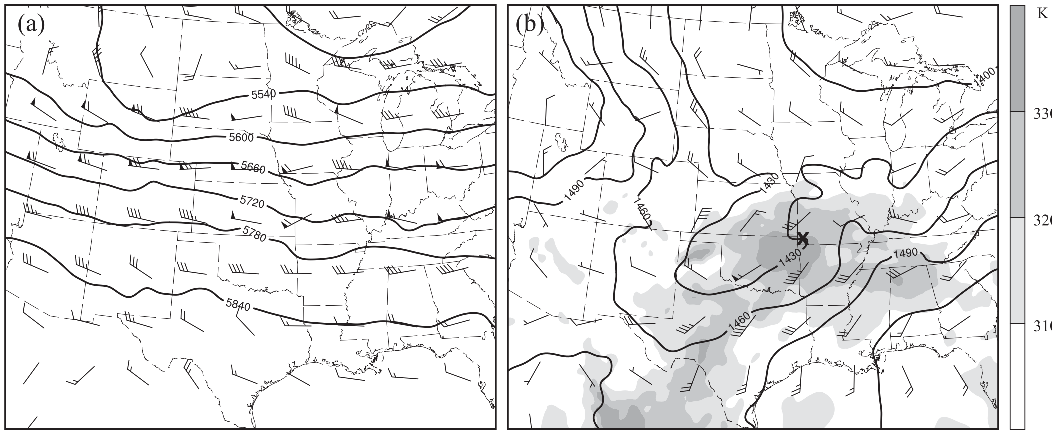

FIG. 3. RUC analysis of total wind and geopotential height at (a) 500 and (b) 850 hPa valid at 1200 UTC 8 May 2009. The equivalent potential temperature (shading) is also shown in (b). Full wind barbs are drawn every 5 m s^{-1} and pennants represent 25 m s^{-1}. The crisscross at southwest Missouri in (b) indicates the location of the sounding in Fig. 4.

and track the observed MVs in this study. The velocity data are first quality controlled and dealiased using an automated procedure from the Advanced Regional Prediction System (ARPS; Brewster et al. 2005). Bow-echo MVs are detected from the radar radial velocity data using a linear least squares derivatives (LLSD) technique, which fits the radial velocity locally by a linear combination of azimuthal shear (AS) and radial shear (Smith and Elmore 2004; Newman et al. 2013). The LLSD method is more tolerant of the noise in radar velocity data in comparison to the traditional methods. The NCEP 13-km RUC (Benjamin et al.

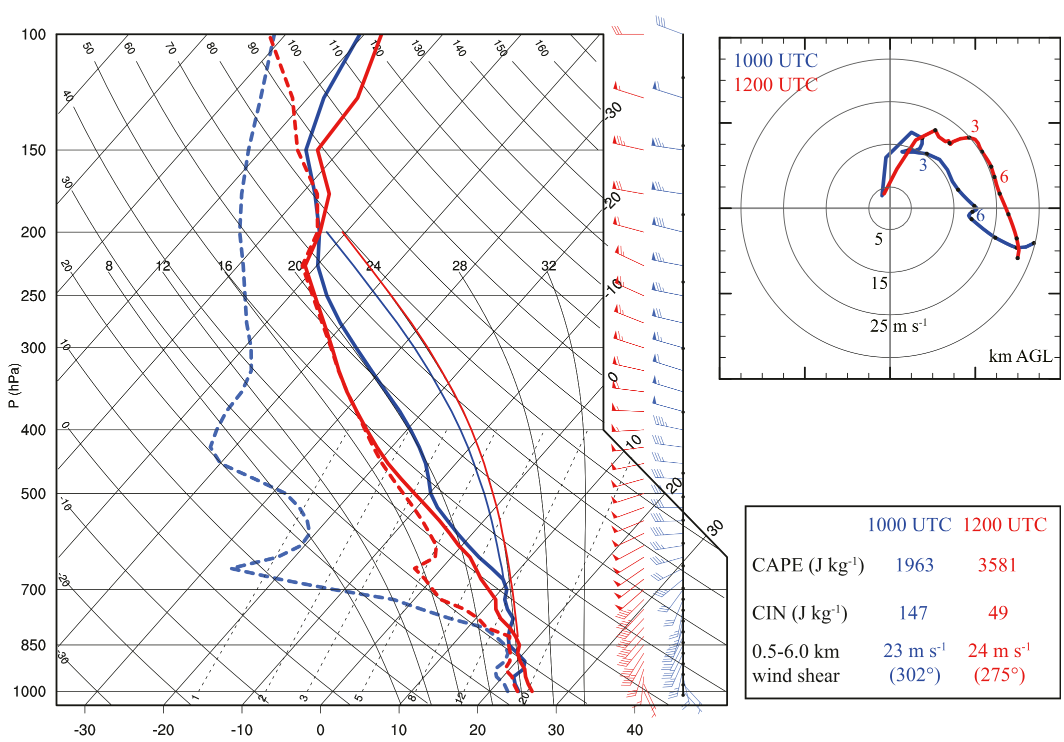

FIG. 4. Soundings and hodographs at southwest Missouri (see Fig. 3) valid at 1000 (blue) and 1200 UTC (red) 8 May 2009 from the RUC analyses. Full wind barbs are drawn every 5 m s^{-1} and pennants represent 25 m s^{-1}. The CAPE and vertical wind shear (magnitude and direction) are shown in the bottom right.

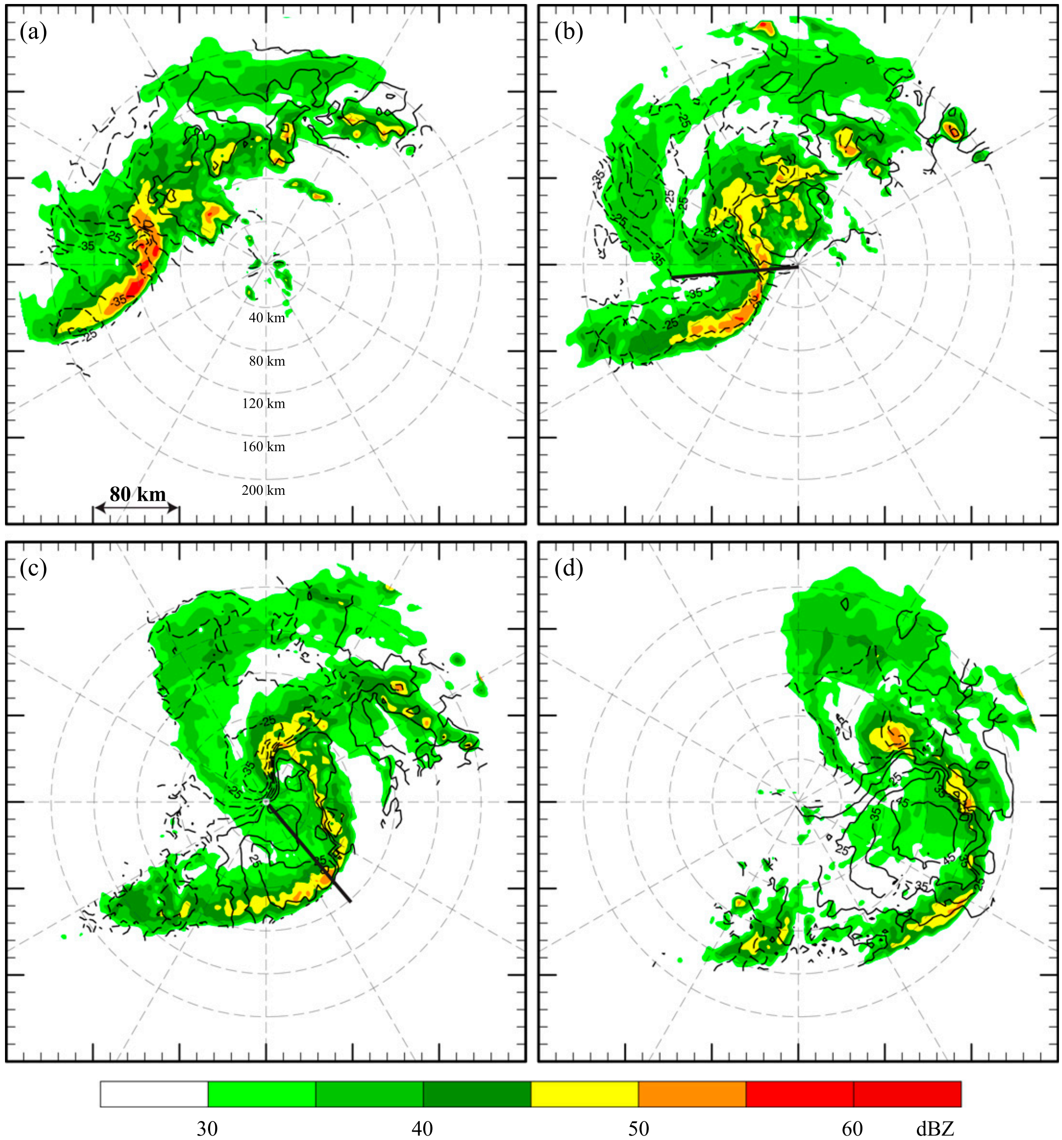

FIG. 5. Radar ground-relative radial velocity (contours) and reflectivity (shading) at the lowest elevation scan at (a) 1203, (b) 1244, (c) 1344, and (d) 1444 UTC. Radial velocities are labeled from 25 m s^{-1} at an interval of 10 m s^{-1}. Thick solid lines in (b) and (c) denote the position of the vertical cross section shown in Fig. 6.

2004) analyses are used to investigate the environmental conditions of the system.

A real-data, high-resolution simulation is performed for the 8 May 2009 bow echo, using the Advanced Research Weather Research and Forecasting (WRF) Model (WRF-ARW; Skamarock et al. 2005). Two nested domains are set for the model, which are two-way interactive (Fig. 2). The outer domain has 901 × 673 horizontal grid points with 4-km grid spacing and has the same configuration as the control member of the CAPS real-time storm-scale ensemble forecasts (SSEF; Xue et al. 2009; Kong et al. 2009). The nested inner domain uses a much finer resolution of 0.8 km with 1401 × 1081 horizontal grid points to better resolve the MVs. *This study focuses predominantly on the output of the 0.8-km domain*. Both domains have 51 vertical levels, with the level interval increasing from ~60 m near the surface to ~600 m at the 50-hPa model top. Both grids employ the Thompson microphysics scheme (Thompson et al. 2008), the Mellor–Yamada–Janjic planetary boundary layer scheme (Janjic 1994), the Goddard shortwave radiation scheme (Tao et al. 2003), and the NCEP–Oregon State University–Air Force–NWS Office of Hydrology (Ek et al. 2003) Noah land surface model (LSM).

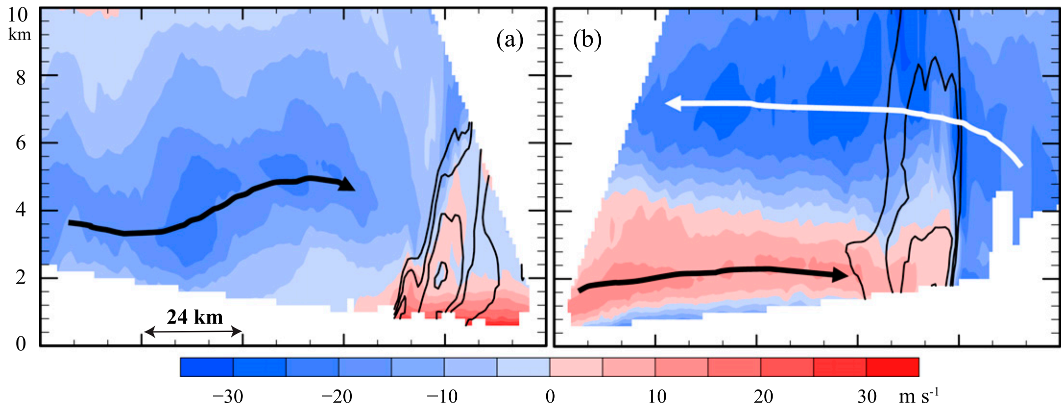

FIG. 6. Radar reflectivity (contours) and storm-relative radial velocity (shading) within a vertical cross section near the bow apex (see Figs. 5b,c) at (a) 1244 and (b) 1344 UTC. Black arrows indicate the RIJ; the white arrow in (b) denotes a front-to-rear jet.

The 4-km model run starts at 0000 UTC 8 May 2009, with the nested domain activated 11 h later at 1100 UTC. The initial condition of the 4-km grid is created by the ARPS 3DVAR/cloud analysis system (Xue et al. 2000, 2003) using the operational NCEP North American Mesoscale Forecast System (NAM) analysis at 0000 UTC 8 May 2009 as the background. Radar data and mesoscale surface observations are assimilated into the initial condition. More details on the creation of the initial conditions can be found in Xue et al. (2009). The NAM forecasts at 3-h intervals are used for the lateral boundary conditions for the outer grid. The inner grid starts from the interpolated 11-h forecast of the 4-km grid.

3. Overview of the 8 May 2009 bow echo

a. Environmental conditions

As pointed out by Coniglio et al. (2011), there was weak synoptic-scale forcing in the pre-MCS environment on 8 May 2009. The synoptic-scale forcing was also weak at 1200 UTC when the system evolved into a large bow echo. Broad westerlies of >20 m s^{-1} were prominent over the Midwest at 500 hPa (Fig. 3a). At 850 hPa there was a low pressure trough extending from western Oklahoma to southwestern Texas, with high winds (15–22.5 m s^{-1}) on its south-southeast flank (Fig. 3b). Warm, moist air of high equivalent potential temperature (θ_e) was transported by this

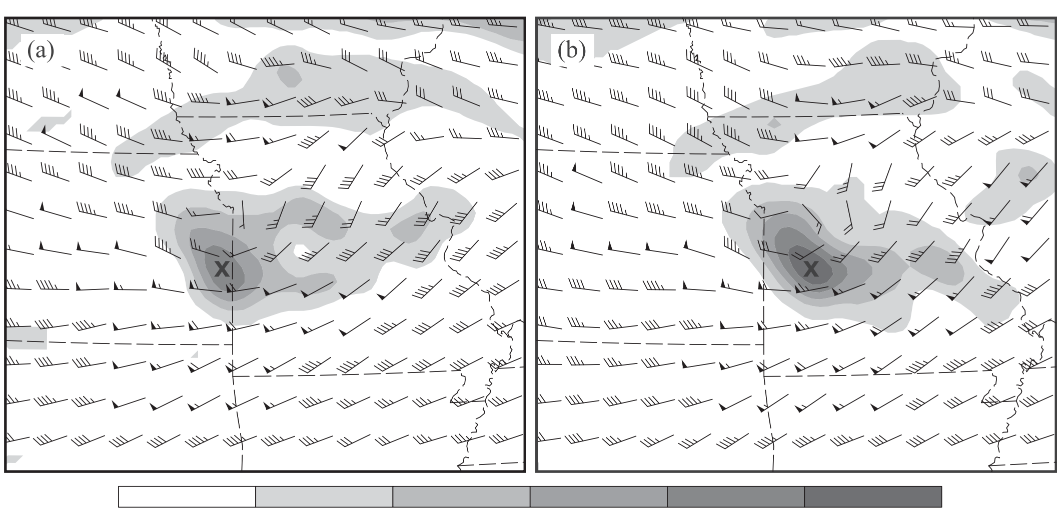

FIG. 7. 500-hPa absolute vertical vorticity (shading) and 600-hPa total wind field from the RUC analysis valid at (a) 1400 and (b) 1500 UTC 8 May 2009. Full wind barbs are drawn every 5 m s^{-1} and pennants represent 25 m s^{-1}. The MCV circulation center at 600 hPa is marked by a black ×.

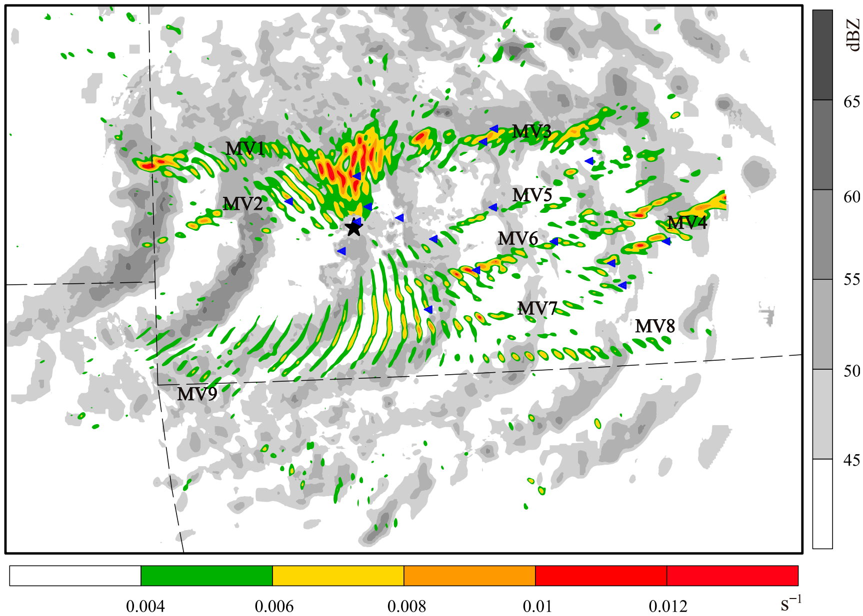

FIG. 8. Radar composite reflectivity (gray shading) and ground-relative tracks of the radial velocity azimuthal shear (color shading) at the lowest elevation between 1203 and 1533 UTC 8 May 2009. Significant MVs are labeled. Filled star indicates the radar location. Blue triangles are the tornadoes reported by the SPC.

strong low-level jet (LLJ) from Texas to Arkansas and Missouri; that is, along the ensuing path of the bow echo.

Figure 4 shows two soundings derived from the RUC analyses at 1000 and 1200 UTC 8 May 2009. The sounding is located at the southwestern corner of Missouri, about 300 km to the east of the large convective system at 1000 UTC, while it is just ahead of the system at 1200 UTC. The environment moistened and cooled as the convective system approached, exhibiting enhanced convective available potential energy (CAPE, from 1963 to 3581 J kg^{-1}), reduced convective inhibition (CIN, from 147 to 49 J kg^{-1}), and lowered level of free convection (LFC, from about 700 to 850 hPa), all of which favored the development of intense convection. In both soundings, the magnitude of the 0.5–6-km vertical wind shear remained around 23–24 m s^{-1}, a value that is conductive to strong and long-lived QLCSs (Weisman 1993). However, given the (approximately) southwest–northeast orientation of the system leading convective line, the line-normal wind shear related to RKW theory was mainly above 3 km AGL, with the low-level wind shear in general parallel to the leading convective line. This is consistent with the findings of Coniglio et al. (2012). Readers are referred to Coniglio et al. (2012) and Weisman et al. (2013) for more detailed discussions on the environment conditions of this bow-echo case.

b. Structure and evolution

The 8 May 2009 central U.S. MCS reached southeastern Kansas around 1200 UTC (see Fig. 1) and evolved into a large bow echo with a horizontal scale in excess of 120 km (Fig. 5a). Large ground-relative radial velocities (GRVr) of over 35 m s^{-1} were observed in connection with a reflectivity notch (Przybylinski 1995) behind the bow-echo apex, implying the presence of an RIJ (Smull and Houze 1987).

Over the next two hours, the large bow echo moved southeastward (Fig. 1) and matured at around 1330 UTC growing to about 240 km in length (Figs. 5b,c). Cyclonic rotation developed on the northern portion of the system (e.g., Evans et al. 2014), as evidenced by the reflectivity spirals extending north-northwestward. In the mature stage of the bow echo, a hook-shaped echo developed at the northern end of the primary convective line, in association with a positive–negative radial velocity couplet (Fig. 5c). Meanwhile, a RIJ that appeared to be elevated at 1244 UTC (Fig. 6a) showed a descent to about 2 km, along with a front to rear jet (Houze et al. 1989) forming at a high altitude of about 7 km (Fig. 6b). Rearward-propagating flow was also found below the RIJ, which reflects the divergent nature of the descending RIJ and rearward spreading of cold pool air along the surface.

The overall system changed its direction to move east-northeastward at about 1400 UTC and began to decay

TABLE 1. Features of radar-detected MVs.

MV	Initial location relative to apex	Initial time (UTC)	Lifetime (min)	Movement	Max AS (s^{-1})	Tornadic
1	N	1131	106	E	0.014	No
2	N	1158	77	NE	0.010	No
3	N	1349	94	E	0.014	Yes
4	N	1400	78	NE	0.013	Yes
5	N	1335	77	NE	0.010	Yes
6	N	1335	98	NE	0.013	Yes
7	N	1335	69	NE	0.013	Yes
8	S	1335	89	E	0.010	No
9	S	1208	54	SE	0.007	No

afterward (Fig. 1). Vigorous convection nearly ceased along the leading edge of the system by 1530 UTC, leaving only a few convective cells at the northern end (Fig. 1). Despite the weakening of the convective system, a midlevel MCV developed at its northern portion (Weisman et al. 2013; Evans et al. 2014), as shown in Fig. 7. The maximum absolute vertical vorticity (ζ_a) increased by ~20% at 1500 UTC (Fig. 7b) compared to 1400 UTC (Fig. 7a). Note that the convective system in the RUC analysis was a couple of hundred kilometers to the west of observations.

4. Radar-detected mesovortices within the bow-echo system

Low-level, convective-scale circulations in the bow echo can be readily detected from the radial velocity AS field at the lowest elevation. However, most circulations are weak, disorganized, and short lived; only a few are recognized as significant MVs with coherent structure and considerable lifetime. These MVs in general have a peak azimuthal shear greater than $0.01\,s^{-1}$ and last for more than 30 min.[1] By aggregating the AS at different times, the ground-relative tracks of these MVs are shown in Fig. 8. The general features of these MVs are summarized in Table 1.

MVs are found on both sides of the bow-echo apex. However, most MVs form on the northern portion of the bow echo, with higher intensities and longer lifetimes than their southern counterparts (e.g., MV1 vs MV9). The mean lifetime for these MVs is about 82 min, longer than the 56-min mean lifetime reported in Atkins et al. (2004). Overlaying the SPC tornado reports on the MV tracks shows that some MVs spawn tornadoes in the mature and decaying stage of the system. Particularly, all tornadic MVs occur within the northern portion of the bow echo.

Two nontornadic MVs (MV1 and MV2) are observed on the leading edge of the bow echo at 1203 UTC (Fig. 9a). MV1 occurs well north of the bow apex and can be traced back to at least 1130 UTC (not shown). MV1 generally moves eastward, with a peak AS intensity of $0.014\,s^{-1}$ at 1203 UTC. In contrast, MV2 forms near the bow apex at about 1200 UTC and moves toward the northeast, maturing with a moderate AS of about $0.01\,s^{-1}$ at 1221 UTC (Fig. 9b). Later MV2 merges with three cyclonic vortices to its southeast (Fig. 9c), forming an elongated shear zone along the leading edge of the northern bow echo. This shear zone then merges with MV1 at 1307 UTC and thus becomes more elongated (Fig. 9d). It is segmented into isolated vortices again by 1317 UTC (Fig. 9e), however. Later, as a pronounced reflectivity hook develops at the northern end of the bow, a band of enhanced AS (labeled as the "along-hook shear region" in Fig. 9f) is observed on the inner edge of the hook, which contains several embedded vortices.

MV3 forms to the east of the along-hook shear region at about 1350 UTC and persists until 1520 UTC, achieving a peak AS of $0.014\,s^{-1}$ at 1402 UTC (Fig. 9h). In general, MV3 moves eastward along the bow echo's northern end, with two tornadoes observed on its track (Fig. 8). MV4 is also generated on the northern bow echo but at a later time than others. Compared to MV3, MV4 forms closer to the bow apex and moves northeastward, lasting for a shorter lifetime of about 80 min (Fig. 8). Tornadoes are found with MV4 as well (Fig. 8).

MV5 through MV8, can be traced back to an elongated region of azimuthal shear near the bow apex (Figs. 9d,e). By 1335 UTC, this shear zone segments into four MVs: MV5, MV6, MV7, and MV8 (Fig. 9f). MV5, MV6, and MV7

[1] When the large bowing system is far away from the radar station (e.g., before 1200 UTC and after 1400 UTC), the azimuthal shear of radial velocity calculated at the lowest elevation will actually reflect the rotational features at a high altitude (>1 km AGL) rather than near the surface. This may cause a problem in ascertaining the exact beginning and end time of MVs at *low levels*. Additionally, the radial velocity only reflects part information of the full 3D wind field and, hence, the rotational feature of MVs. Because of these uncertainties with the single-Doppler radar-based identification of MVs, the lifetime of MVs shown in Table 1 should be viewed as estimates of their actual lifetime, especially for long-lived MVs.

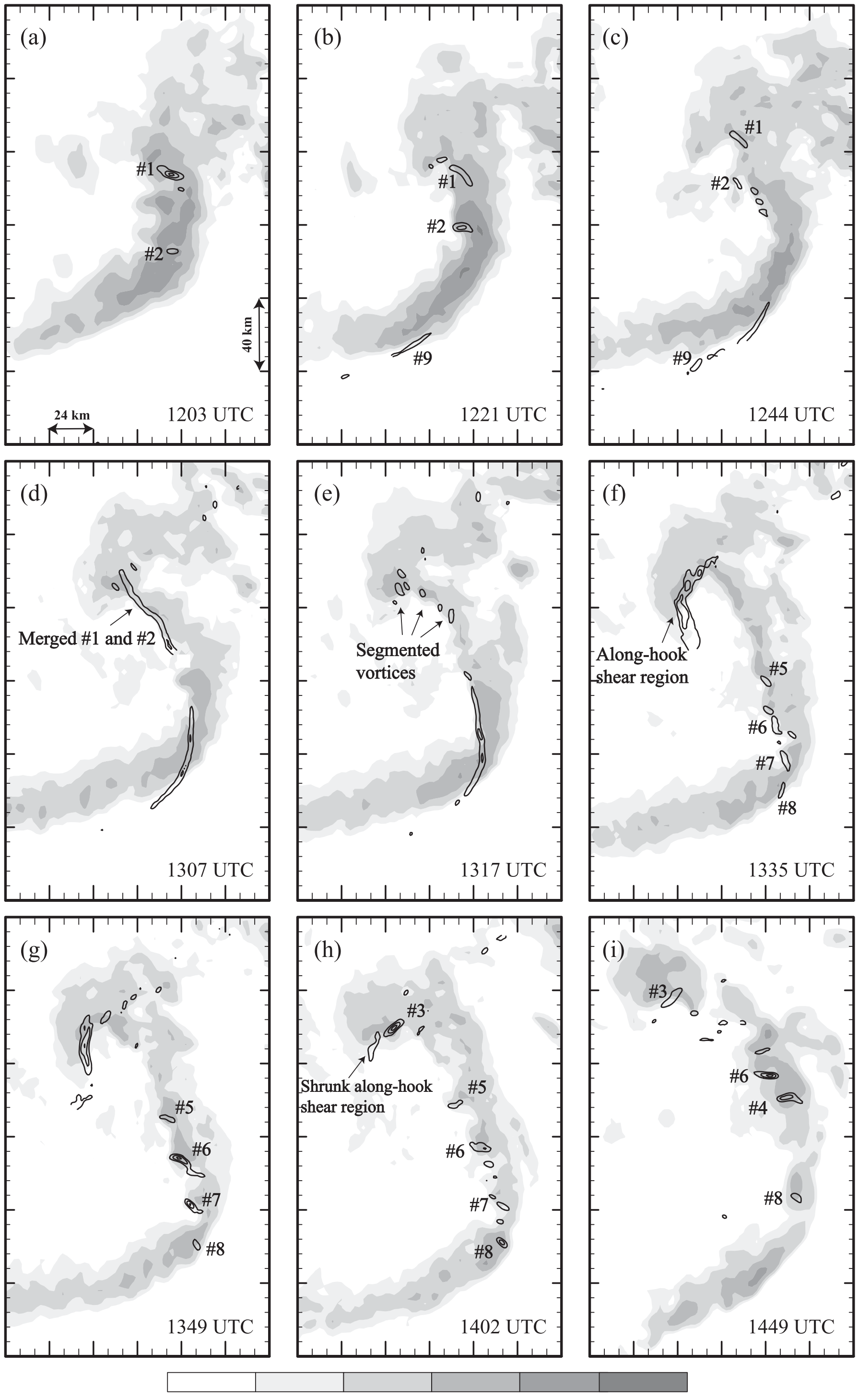

FIG. 9. Radar composite reflectivity (shading) and azimuthal shear (contours, $\geq 0.004\,\mathrm{s}^{-1}$ at $0.004\,\mathrm{s}^{-1}$ interval) of radial velocity at the lowest elevation at (a) 1203, (b) 1221, (c) 1244, (d) 1307, (e) 1317, (f) 1335, (g) 1349, (h) 1402, and (i) 1449 UTC. The plotted domain is 144 km by 240 km.

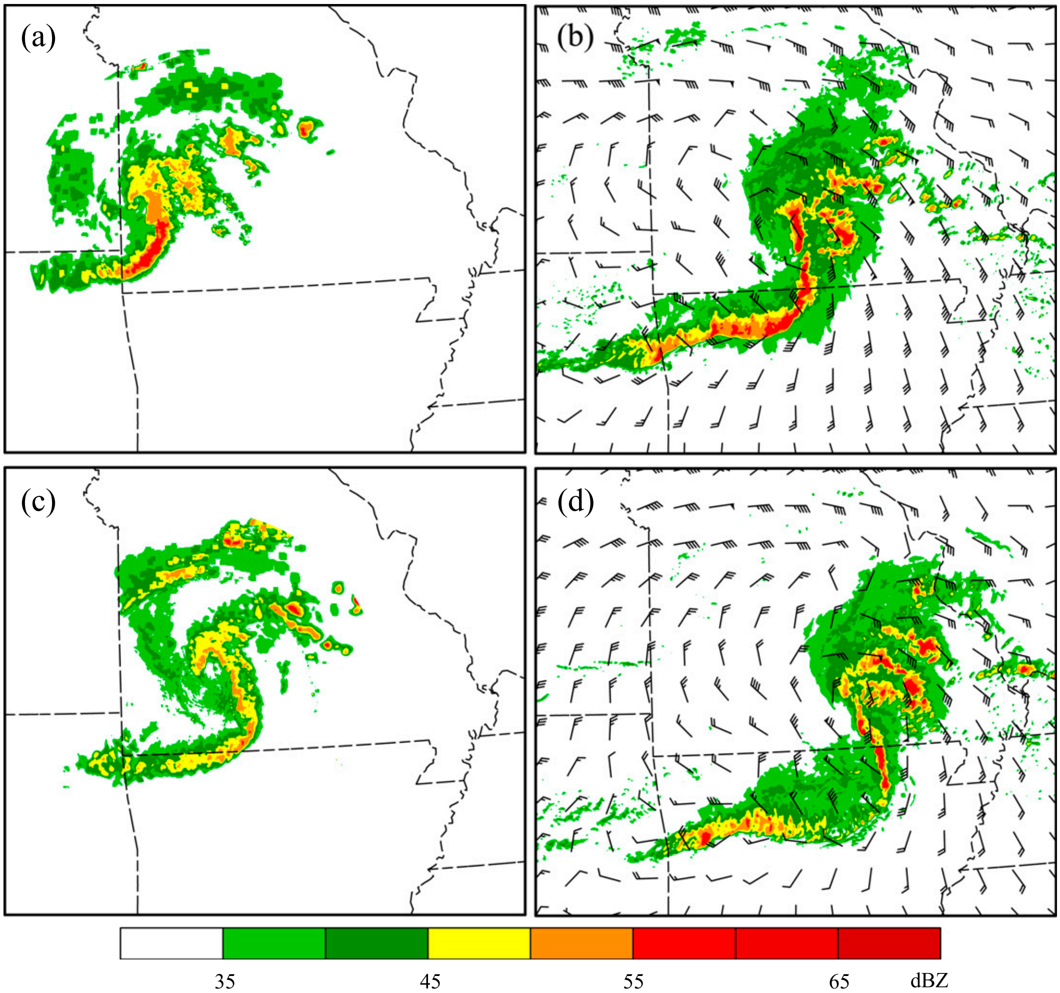

FIG. 10. Comparison between the radar and model-simulated composite reflectivity for the 8 May 2009 central U.S. bow echo. Radar observations at (a) 1231 and (c) 1339 UTC. Model results at (b) 1430 and (d) 1540 UTC. The storm-relative wind fields at 2.5 km AGL are also shown in (b) and (d). Full wind barbs are drawn every 5 m s^{-1} and pennants represent 25 m s^{-1}.

move northeastward and stay north of the bow apex, with tornadoes observed on their tracks (Fig. 8). MV6 and MV7 intensify significantly at 1349 UTC (Fig. 9g). The previously continuous leading convective line tends to be segmented by these strengthened MVs (e.g., Trapp and Weisman 2003). While MV7 weakens with time and becomes undetectable by 1449 UTC (Fig. 9i), MV6 experiences a redevelopment around 1430 UTC and matures again at 1449 UTC. Mergers with nearby vortices are found responsible for the redevelopment of MV6, with its lifetime prolonged notably. Unlike MV5, MV6, and MV7, MV8 is nontornadic and generally moves eastward, staying south of the bow apex. It only shows a moderate increase in intensity, with a maximum AS of about 0.010 s^{-1} at 1402 UTC (Fig. 9h).

MV9 is also nontornadic, forming on the southern bow echo. It moves toward the southeast and stays on the southern bow all the time. MV9 is the weakest and most short lived among the MVs identified (Table 1). It is initiated at about 1208 UTC and dies out around 1300 UTC, maturing with a peak AS of only 0.007 s^{-1} at 1221 UTC (Fig. 9b).

5. Simulated mesovortices within the 8 May 2009 bow echo

a. *Overview of the simulated bow echo*

A time-shifted comparison between the radar and model-simulated composite reflectivity for the 8 May 2009 bow echo is shown in Fig. 10. The model-simulated bow echo occurs about 1–2 h later than reality and is located about 90 km to the southeast (e.g., Figs. 10a,b). The timing and position biases were also noted in the 3-km grid spacing WRF simulation presented in

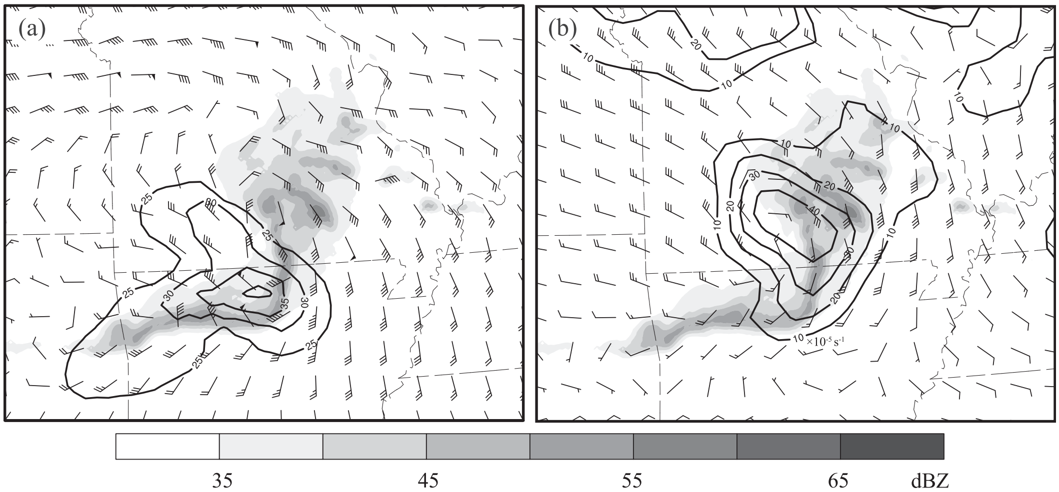

FIG. 11. (a) Ground-relative wind speed (contours, $\geq 25\,\mathrm{m\,s^{-1}}$ at $5\,\mathrm{m\,s^{-1}}$ interval) and storm-relative wind vector at 2.5 km AGL, and (b) 500-hPa absolute vertical vorticity (contours, $\geq 10^{-4}\,\mathrm{s^{-1}}$ at $10^{-4}\,\mathrm{s^{-1}}$ interval) and 600-hPa storm-relative wind vector, from the model output at 1500 UTC. Shadings are the simulated composite reflectivity. Full wind barbs are drawn every $5\,\mathrm{m\,s^{-1}}$ and pennants represent $25\,\mathrm{m\,s^{-1}}$.

Weisman et al. (2013). The general pattern of the simulated bow echo is quite similar to the observations, though the southern end of the leading convective line that is oriented east–west is too extensive in the simulation. In addition, the reflectivity spirals observed in the northern portion of the system are weaker and less extensive in the model. The simulation also lacks a well-defined line-end hook echo (Figs. 10c,d). However, such discrepancies do not necessarily affect the examination of convective-scale MVs using the model output, which

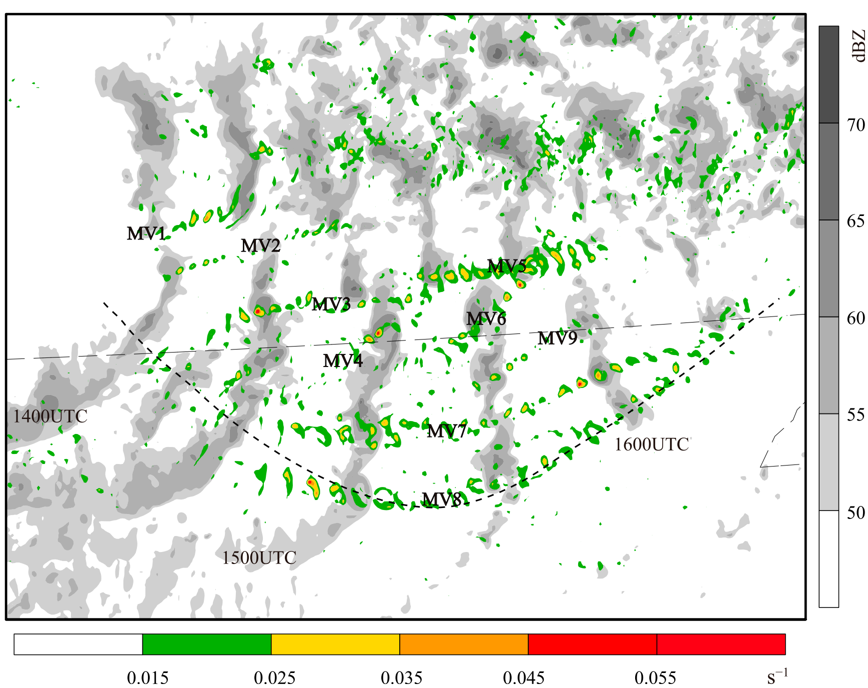

FIG. 12. Composite reflectivity (gray shading) and ground-relative tracks of the maximum absolute vertical vorticity below 2 km AGL (color shading) for the simulated 8 May 2009 central U.S. bow echo from 1400 to 1640 UTC. The thick dashed line denotes the approximate locus of the bow apex. Significant MVs are labeled.

TABLE 2. Features of WRF-simulated MVs.

MV	Location	Initial time (UTC)	Lifetime (min)	Movement	Peak intensity (s^{-1})
1	N	1330	70	NE	0.041
2	N	1330	100	NE	0.026
3	N	1410	75	NE-E	0.050
4	N	1440	40	NE	0.056
5	N	1515	70	ENE	0.035
6	N	1510	50	NE	0.053
7	S	1420	140	SE-NE	0.053
8	S	1420	140	SE-NE	0.050
9	N	1515	50	NE	0.033

is our main goal here. Decay of the entire system begins at about 1530 UTC, with the leading line almost completely dissipated by 1630 UTC; that is, the model bow-echo lifetime is about 1 h shorter than reality. The main mesoscale features of the bowing system are also well captured. An RIJ is found behind the bow apex at 2.5 km AGL, with the peak ground-relative wind speed (GRWS) exceeding 40 m s^{-1} (Fig. 11a). Meanwhile, a midlevel MCV about 200–300 km in diameter is apparent over the northern portion of the bow echo (Fig. 11b), which becomes mature around 1530 UTC.

b. Model-simulated mesovortices within the bow echo

Examination of simulated vertical vorticity reveals the formation of nine persistent MVs with coherent structure within the simulated bow echo.[2] Figure 12 displays the ground-relative tracks of these MVs from 5-min model output, and their general features are summarized in Table 2. The observed shear region along the line-end hook (Fig. 8) is not found in Fig. 12, but many weak vortices do occur at the northern end of the system. In addition, it seems that no elongated shear zones are generated on the leading edge of the system, but this is actually related to the choice of plotted contours—only vertical vorticity $>0.015\,s^{-1}$ is contoured. Continuous contours representing elongated shear zones can be seen when lower-valued contours are drawn (not shown).

MV1 and MV2 are generated well north of the bow apex. Their formation can be traced back to about 1330 UTC (not shown). MV1 persists for about 70 min until 1440 UTC. It mainly moves northeastward along the southern end of a subsystem-scale bow echo, acquiring a peak ζ_a of 0.041 s^{-1} at 1415 UTC (Fig. 13a). MV2 develops south of MV1 and moves parallel to MV1. It lasts for a longer time to about 1510 UTC. MV3 develops near the bow apex at 1410 UTC and soon matures at 1430 UTC (Fig. 13b) with a strong ζ_a up to 0.050 s^{-1}. MV3 then weakens with time and finally merges with MV4 and MV5 at 1525 (Fig. 13e) and 1530 UTC, respectively (not shown).

MV4 is a northeastward-moving vortex that forms southeast of MV3 at 1440 UTC. It develops into a strong vortex of comparable intensity to MV3 at 1500 UTC (Fig. 13c). MV4 is short lived as it is quickly merged with MV3. MV5 is generated a little north of MV3 around 1515 UTC. MV5 initially intensifies to gain a moderate ζ_a of 0.033 s^{-1} at 1540 UTC (Fig. 13f), followed by a weakening until 1555 UTC. It then reintensifies and matures again at 1610 UTC (Fig. 13i). The redevelopment of MV5 is caused by merger with MV6 at 1600 UTC (Fig. 13h). MV6 initiates southeast of MV5 at about 1510 UTC, also moving northeastward. It matures with a large ζ_a of 0.053 s^{-1} at 1550 UTC (Fig. 13g), about 10 min before merging with MV5.

MV7 and MV8 are generated just south of the bow apex. They are of the longest lifetime among the identified MVs, lasting for more than 2 h. Both of them move consistently with the system, producing two distinct, nearly parallel ground-relative tracks (Fig. 12). MV8 remains close to the apex, while MV7 is located about 15–25 km to the north. The peak intensity of MV7 occurs in the late bow-echo stage at 1555 UTC (not shown), showing a peak ζ_a of 0.053 s^{-1}. MV8 reaches peak intensity at 1450 UTC with ζ_a of 0.050 s^{-1} (Fig. 13c). Afterward, MV8 generally maintains a weak-to-moderate intensity until merging with MV7 at about 1620 UTC (Fig. 12). MV9 is generated concurrently with MV6 and also moves northeastward (Fig. 12). The peak ζ_a of MV9 is 0.033 s^{-1} at 1540 UTC (Fig. 13f). MV9 maintains its identity to 1605 UTC, experiencing no merger with any other vortex. Moreover, the MVs north of the bow apex tend to move rearward along the leading convective line as the line moves generally to the east.

c. Relationship between observed and simulated mesovortices

Even though one cannot make one-to-one comparison between the observed and simulated MVs, there are

[2] To distinguish from other weak MVs, significant MVs are identified with a peak vertical vorticity $>0.035\,s^{-1}$. This threshold depends on the model grid resolution. For higher resolution (e.g., 100 m) the peak vertical vorticity of MVs will readily exceed 0.035 s^{-1}.

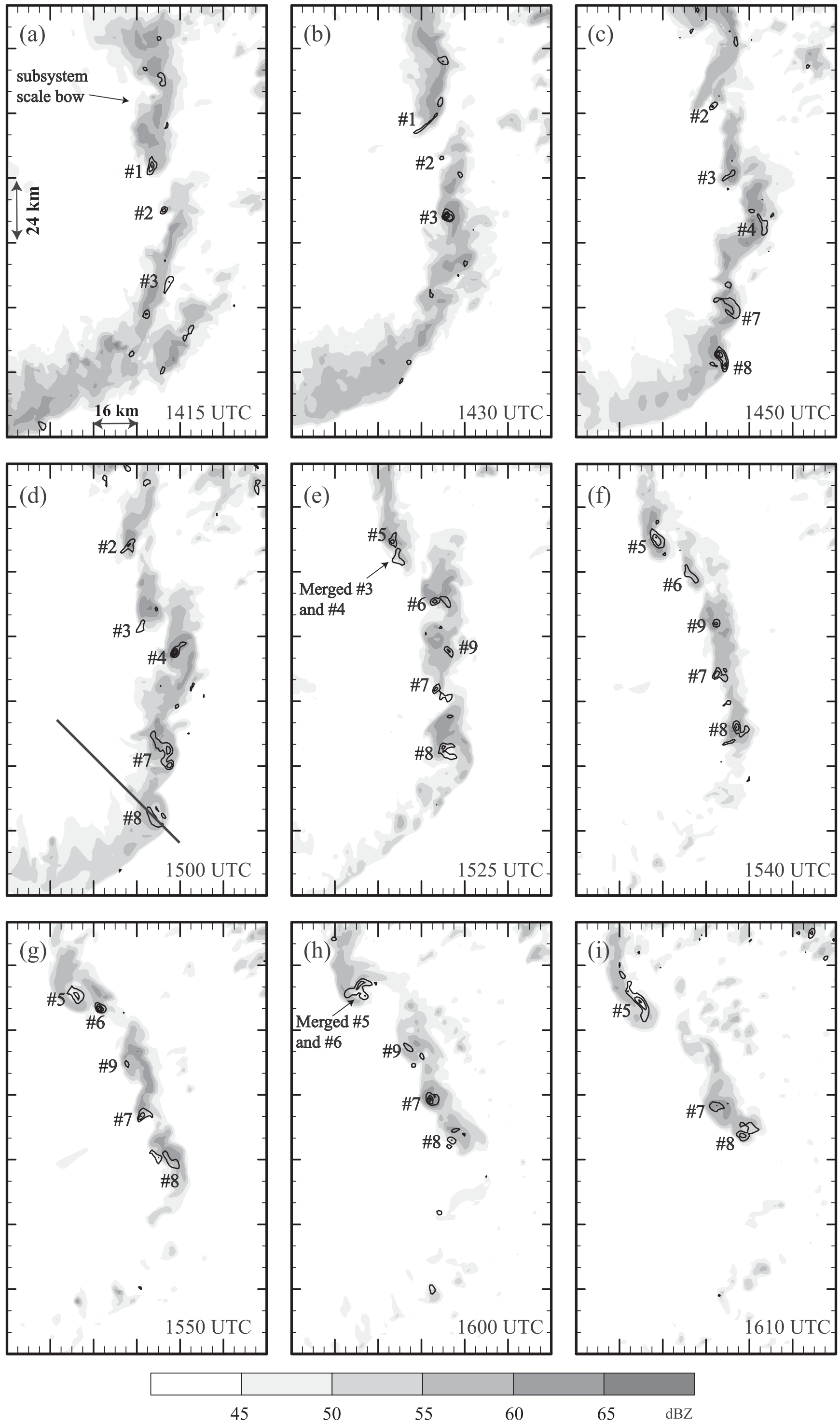

FIG. 13. Model composite reflectivity (shading) and maximum absolute vertical vorticity below 2 km AGL (contours, $\geq 0.015\,\mathrm{s^{-1}}$ at $0.010\,\mathrm{s^{-1}}$ interval) at (a) 1415, (b) 1430, (c) 1450, (d) 1500, (e) 1525, (f) 1540, (g) 1550, (h) 1600, and (i) 1610 UTC. The plotted domain is 96 km by 160 km. The solid line in (d) indicates the approximate position of the vertical plane shown in Fig. 16.

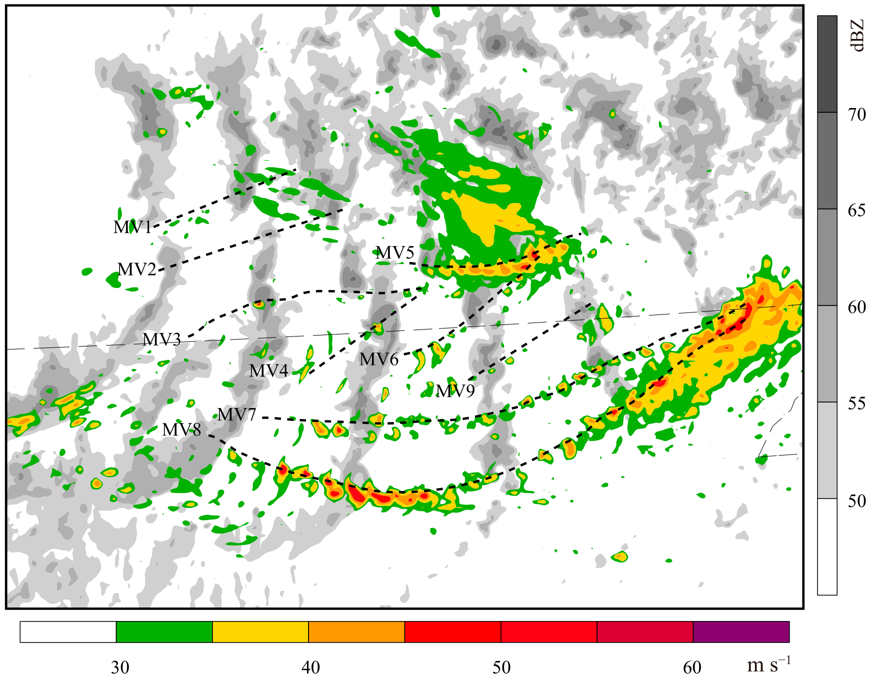

FIG. 14. As in Fig. 12, but that the color shading is for the ground-relative wind speed at 0.2 km AGL. Dashed lines are the tracks of MVs.

many common characteristics between the two sets of MVs. They are similar enough to let us believe that the MVs in the model form through similar physical processes as in the nature. An important goal of this paper is to establish the physical credibility of the model-simulated bow echo and the associated MVs so as to lay a foundation for a detailed diagnostic study of the mesovortex genesis mechanism in a companion paper (Xu et al. 2015).

The simulated and observed MVs resemble each other in three key areas:

1) MVs form on both sides of the bow apex but more predominantly on the northern half of the bow echo. The northern-bow MVs possess stronger rotation and longer lifetimes. This north–south asymmetry, which appears to have been first noted by Weisman and Trapp (2003) in their idealized simulations, is also apparent in radar observations (e.g., Atkins et al. 2004, 2005). It is probably caused by the along-line variation of thermodynamic instability and ambient wind shear (Wheatley and Trapp 2008). Large CAPE and wind shear favor the formation of strong, long-lived MVs. Indeed, the RUC analyses exhibit a greater 3–6-km vertical wind shear ahead of the northern half of the bow echo than that in front of the southern bow from 1200 to 1500 UTC (not shown).
2) Vortex mergers between same-signed vortices are prevalent in both observation and simulation, which also agrees with the results of idealized simulations (Weisman and Trapp 2003; Atkins and St. Laurent 2009a). The MVs can grow upscale through vortex mergers. Vortex mergers are also found to be responsible for the redevelopment of some MVs in the late stage of the large bow echo, with their lifetime prolonged considerably.
3) In both observation and simulation, the most significant MVs are found to form at (or near) the bow apex. These MVs move consistently with the large bowing system and persist for a considerable lifetime, developing a great vertical vorticity while maturing. This is likely the result of the system RIJ at the bow apex (see Figs. 6 and 12a). As studied by Atkins et al. (2005), tornadic MVs are prone to form with or after the genesis of the RIJ, at a location on the gust front where the convergence is enhanced by the descending RIJ.

6. Generation of near-surface high winds within the simulated bow echo

Damaging straight-line winds near the surface have been observed within QLCSs. High winds are also found in our simulated bowing system. Unfortunately, surface wind speed is not directly available in radar observations. Figure 14 shows the tracks of GRWS at 0.2 km

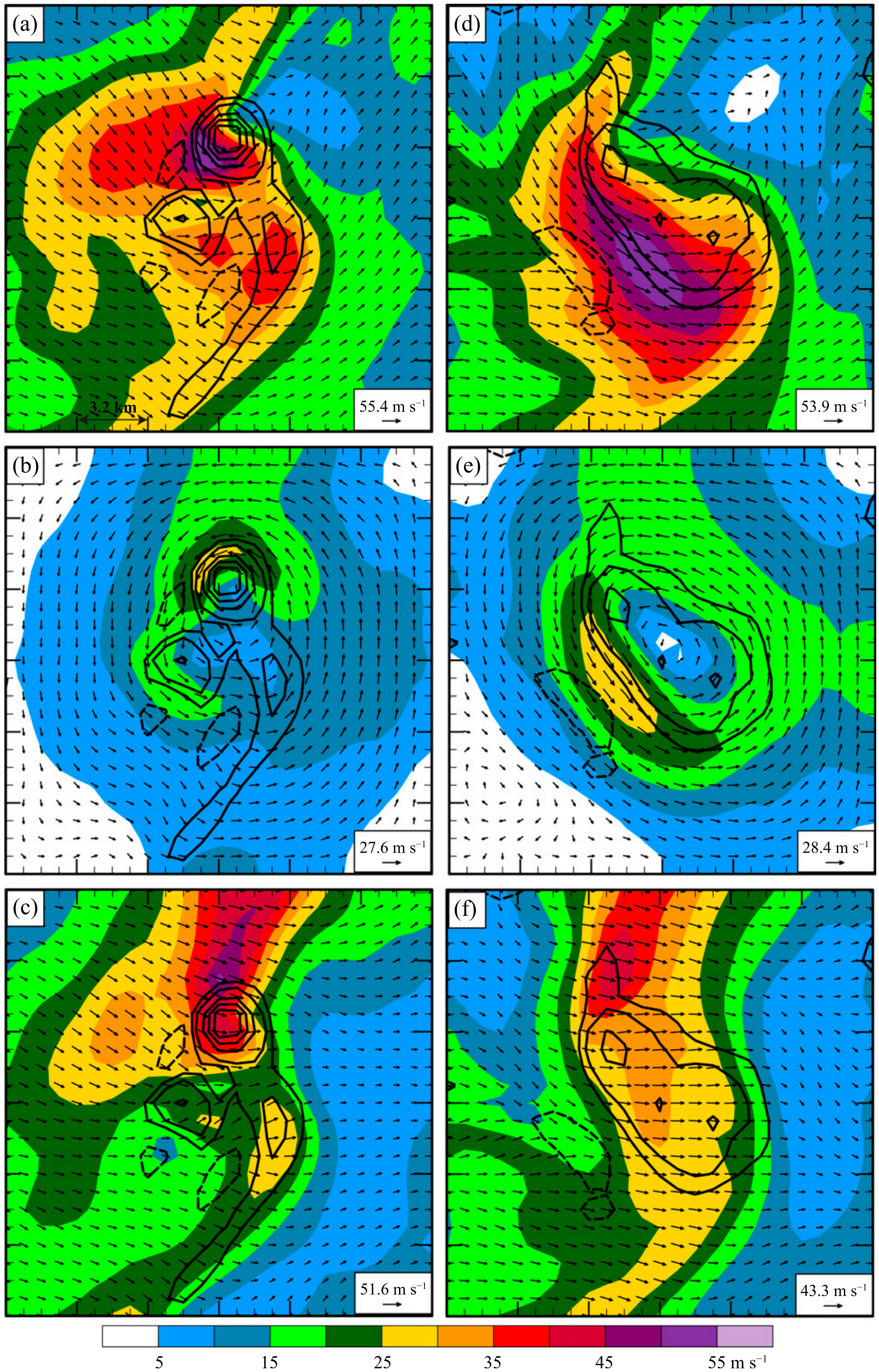

FIG. 15. Decomposition of the (a) total ground-relative wind into (b) mesovortex-induced flow and (c) environmental flow at 200 m AGL at 1450 UTC. (d)–(f) As in (a)–(c), but for the wind at 1500 UTC. Vectors and shadings are for the ground-relative wind field and the corresponding wind speed. Black contour lines denote the simulated vertical vorticity at 200 m AGL at contour values of -0.005, 0.005, 0.01, 0.02, 0.03, and 0.04 s^{-1}, with dashed lines for negative values. The plotted domain is 19.2 km by 19.2 km.

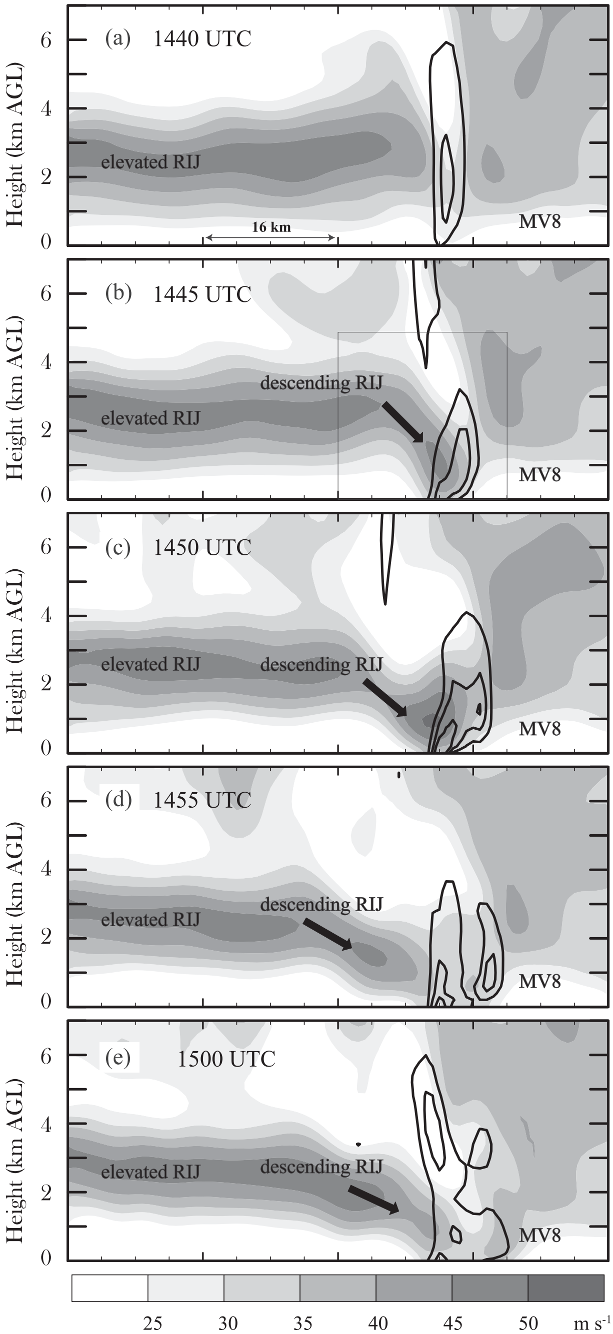

FIG. 16. Model ground-relative wind speed (shading) and vertical vorticity (contours, $\geq 0.01\,s^{-1}$ at $0.01\,s^{-1}$ interval) in the vertical plane through MV8, orientated in a direction approximately normal to the bow-echo gust front at (a) 1440, (b) 1445, (c) 1450, (d) 1455, and (e) 1500 UTC. The approximate position of the vertical cross section is indicated as a black solid line in Fig. 13d. The black box in (b) indicates the domain shown in Fig. 17.

AGL from 1400 to 1640 UTC of our simulation. High winds are mainly produced by the northern half of the bow echo (including the bow apex) during its mature and decaying stages in the simulation. This is in agreement with the SPC report of high winds (see Fig. 1). Moreover, as noted in Atkins and St. Laurent (2009a), not all MVs are associated with damaging winds. GRWSs at 0.2 km AGL are in general smaller than $35\,m\,s^{-1}$ for MV1, MV2, and MV3, while severe winds greater than $45\,m\,s^{-1}$ are found with the remaining MVs. High winds are more persistent for MV5, MV7, and MV8, showing three continuous high-wind tracks. The most severe winds are found with MV8 near the apex where two swaths of strong winds are produced. The first swath forms during the bow echo mature stage from 1450 to 1520 UTC. It is about 80 km in length and 12 km in width, with the peak GRWS $> 55\,m\,s^{-1}$. The second high-wind swath is found between 1610 and 1640 UTC, during the system weakening stage. It is somewhat weaker compared to the first swath, with most winds less than $45\,m\,s^{-1}$. However, the second swath is much broader in areal extent, perhaps due to the merger of MV8 and MV7.

a. High winds and mesovortices

High winds with bow-echo MVs have been attributed to the superposition of the mesovortex flow and the system flow in which it is embedded; as a result, the local wind maxima form on the side of the MV where the system flow is in the same direction as the vertical flow (e.g., Wakimoto et al. 2006b). To quantify the contribution from the MV, the nondivergent part of the horizontal velocity is retrieved from the vertical vorticity field by solving a two-dimensional Poisson equation (e.g., Atkins and St. Laurent 2009a). For example, in MV8 at 1450 UTC near-surface high winds are generally located on its southwest periphery (Fig. 15a). The MV-induced flow accounts for a notable fraction (30%–50%) of these high winds (Fig. 15b), and the position of the high-wind center is displaced northward when MV8 is removed (Fig. 15c). These findings are consistent with the results of Atkins and St. Laurent (2009a, see their Fig. 12). Similar results can be found when examining the high winds associated with MV8 at 1500 UTC (Figs. 15d–f) although MV8 has weakened markedly at this time. Overall, these results show that low-level MVs within QCLSs can help increase the severity of the convective system.

b. High winds and the RIJ

As evidenced in Fig. 15, it is evident that a great fraction of the near-surface high winds comes from the ambient translational flow. Given the location of MV8 (i.e., near the bow apex where the system-scale RIJ is present), the high winds in proximity to MV8 are likely promoted by the descent of the RIJ. Figure 16 shows the time evolution of the RIJ in the vertical plane through

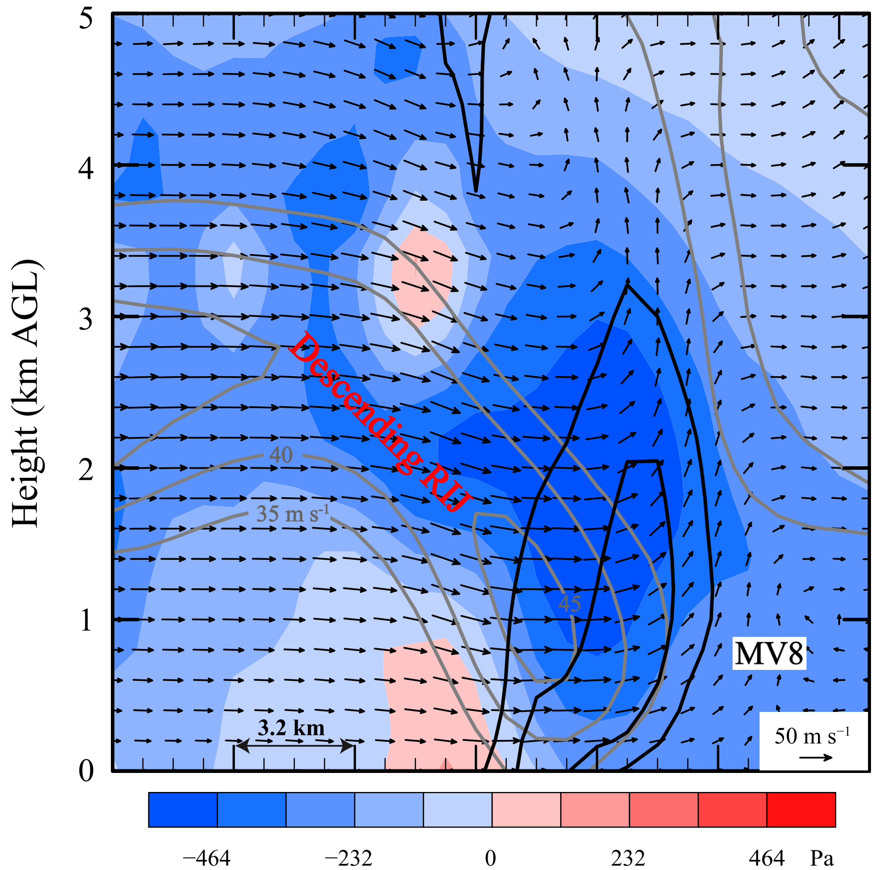

FIG. 17. Vertical cross section of model pressure perturbation (shading) at 1445 UTC. Also shown are the vertical vorticity (black contours at values of 0.01 and $0.02\,s^{-1}$) and ground-relative wind speed (gray contours). The position of the vertical plane is indicated as black box in Fig. 16b.

MV8, orientated in a direction approximately normal to the bow-echo gust front. At 1440 UTC (Fig. 16a), the RIJ is elevated at about 3 km AGL, with a maximum GRWS over $45\,m\,s^{-1}$. MV8 is fairly deep at this time, extending from the surface to about 6 km AGL, with the vertical vorticity maximum located at 2 km AGL. At 1445 UTC (Fig. 16b), the RIJ exhibits a notable descent toward the surface immediately behind MV8. At this time, the previously erect MV8 is cut into two parts around 3 km AGL, along with an evident lowering of the vortex center. A localized positive pressure perturbation is present at the descending point of the RIJ at about 3.5 km AGL (Fig. 17), which is likely due to flow blocking as the RIJ impinges upon the intense updrafts at the leading convective line (in accordance with the Bernoulli theorem that a deceleration of airflow will result in an increase in pressure). In contrast, a broader and stronger pressure perturbation minimum develops in the upper portion of MV8, as compared to the positive pressure perturbation. This negative pressure perturbation is likely due to the strong rotation of the mesovortex MV8 where the cyclostrophic balance creates low vortex center pressure (Trapp and Weisman 2003). Given the pressure perturbation pattern, a downward-directed perturbation vertical pressure gradient force is created, acting to push down the RIJ. (Hereafter, "vertical pressure gradient force" refers to "perturbation vertical pressure gradient force.") This negative vertical pressure gradient force is therefore believed to be dynamically induced, which will be discussed further later. Five minutes later at 1450 UTC (Fig. 16c), the descending RIJ behind MV8 gets stronger, exhibiting a localized GRWS maxima $>50\,m\,s^{-1}$. Moreover, the vertical vorticity of MV8 increases near the surface. Over the next 10 min (Figs. 16d,e), the descending of the RIJ is still evident behind MV8. Note that the near-surface vorticity of MV8 decreases with time during this period.

That severe near-surface winds are promoted by the descent of the RIJ can be seen clearly by tracking the parcel trajectories backward with time. Figure 18 shows the 10-min (1450–1440 UTC) backward trajectories[3] for sampled parcels populating the high-wind region southwest of MV8 at 1450 UTC. Of all the 189 parcels with GRWS $> 40\,\mathrm{m\,s^{-1}}$ at 200 m AGL, 123 of them descend from above 1 km AGL, including 104 (80) from over 1.5 (2) km AGL. These parcels mainly come from about 10 km north of MV8 (i.e., they originate from the RIJ because MV8 is located at the southeast tip of the RIJ; Figs. 19a,c). Another mesovortex MV7 also forms near the RIJ but to the opposite side. At 1440 UTC (Fig. 19a) a localized downdraft is present in the western part of MV8. This downdraft extends upward to about 4 km AGL, with the peak downward motion $>8\,\mathrm{m\,s^{-1}}$ between 1.5 and 3 km AGL (i.e., close to the RIJ core; Fig. 19b). Similarly, MV7 is also accompanied with a localized downdraft. Between MV8 and MV7, weak downdrafts $<4\,\mathrm{m\,s^{-1}}$ are found below about 2.5 km AGL but with updrafts aloft (Fig. 19b). These downdrafts have intensified by 1445 UTC (Fig. 19c), showing an increase in their vertical extent (Fig. 19d).

c. *Pressure diagnostics for RIJ*

To better understand the descent of the RIJ, vertical momentum budgets are performed in accordance with the following equation for deviations from a base-state atmosphere in hydrostatic balance (Doswell and Markowski 2004):

$$\frac{Dw}{Dt} = -\frac{1}{\overline{\rho}}\frac{\partial p'_d}{\partial z} + \left(-\frac{1}{\overline{\rho}}\frac{\partial p'_b}{\partial z} + b\right) + F = -\frac{1}{\overline{\rho}}\frac{\partial p'_d}{\partial z} + B + F. \tag{1}$$

Here p'_d is the dynamic pressure perturbation (with respect to the base state pressure), p'_b is the pressure perturbation due to buoyancy, b is the *thermal* buoyancy given by

$$b = g\left(\frac{\theta'}{\overline{\theta}} + 0.61q'_v - q_w\right), \tag{2}$$

where q'_v is the perturbed water vapor mixing ratio, q_w is the sum of both liquid and solid hydrometeor mixing ratios in the air, and F represents the mixing term including subgrid-scale turbulence and surface friction. All other variables have their usual meanings. The decomposition of the total pressure perturbation into contributors from dynamics (p'_d) and buoyancy (p'_b) follows that of Rotunno and Klemp (1985) as well as Trapp and Weisman (2003). As discussed in Doswell and Markowski (2004), B is independent of the choice of the base state such that it denotes the total buoyancy, or *effective* buoyancy, felt by an air parcel. The dynamic and buoyant pressure perturbations can be separately diagnosed from the following two three-dimensional (3D) Poisson equations along with appropriate

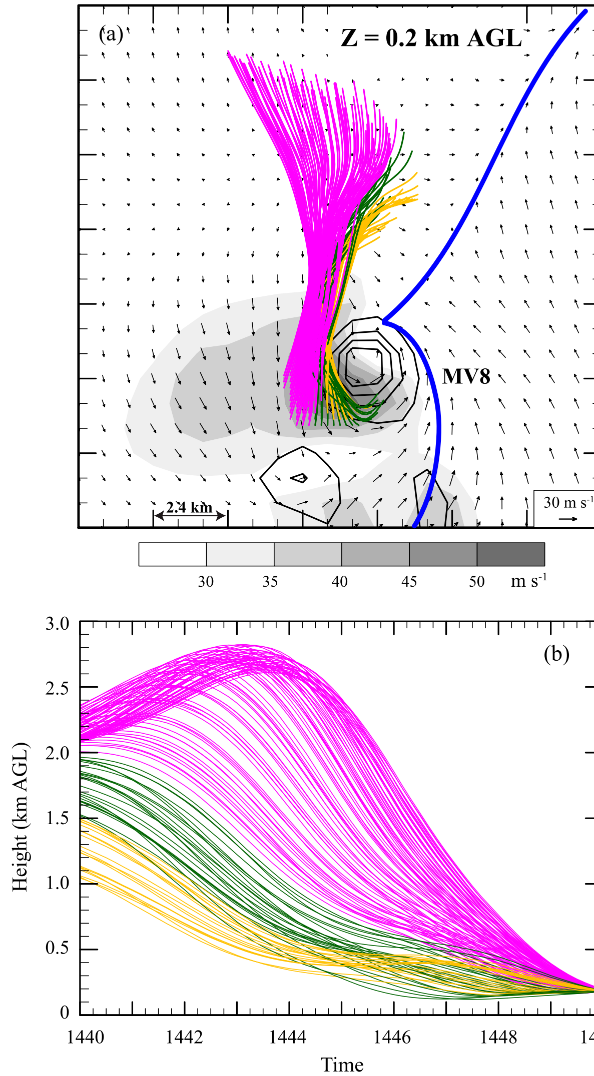

FIG. 18. (a) The 10-min (1450–1440 UTC) backward trajectories for parcels populating the high-wind region ($>40\,\mathrm{m\,s^{-1}}$) near MV8 at 200 m AGL. Only parcels with an initial height (i.e., the height at 1440 UTC) greater than 1 km AGL are shown. Parcel trajectories are colored yellow, green, and pink when the parcel's initial height is greater than 1, 1.5, and 2 km AGL, respectively. The vertical vorticity (contours, $\geq 0.01\,\mathrm{s^{-1}}$ at $0.01\,\mathrm{s^{-1}}$ interval) and storm-relative wind field (vector) at 200 m AGL are also shown. The blue line indicates the position of the gust front that is drawn manually. (b) Height of parcels in (a) from 1440 to 1450 UTC.

[3] Backward trajectories are calculated by using the trajectory program within the ARPS model system (i.e., ARPSTRAJC), which employs the second-order trapezoidal scheme with iterations for time integration. To utilize this program, the WRF gridded data are first converted to the ARPS gridded data according to the program WRF2ARPS also within ARPS. Then the trajectories are calculated with model history files at 10-s intervals.

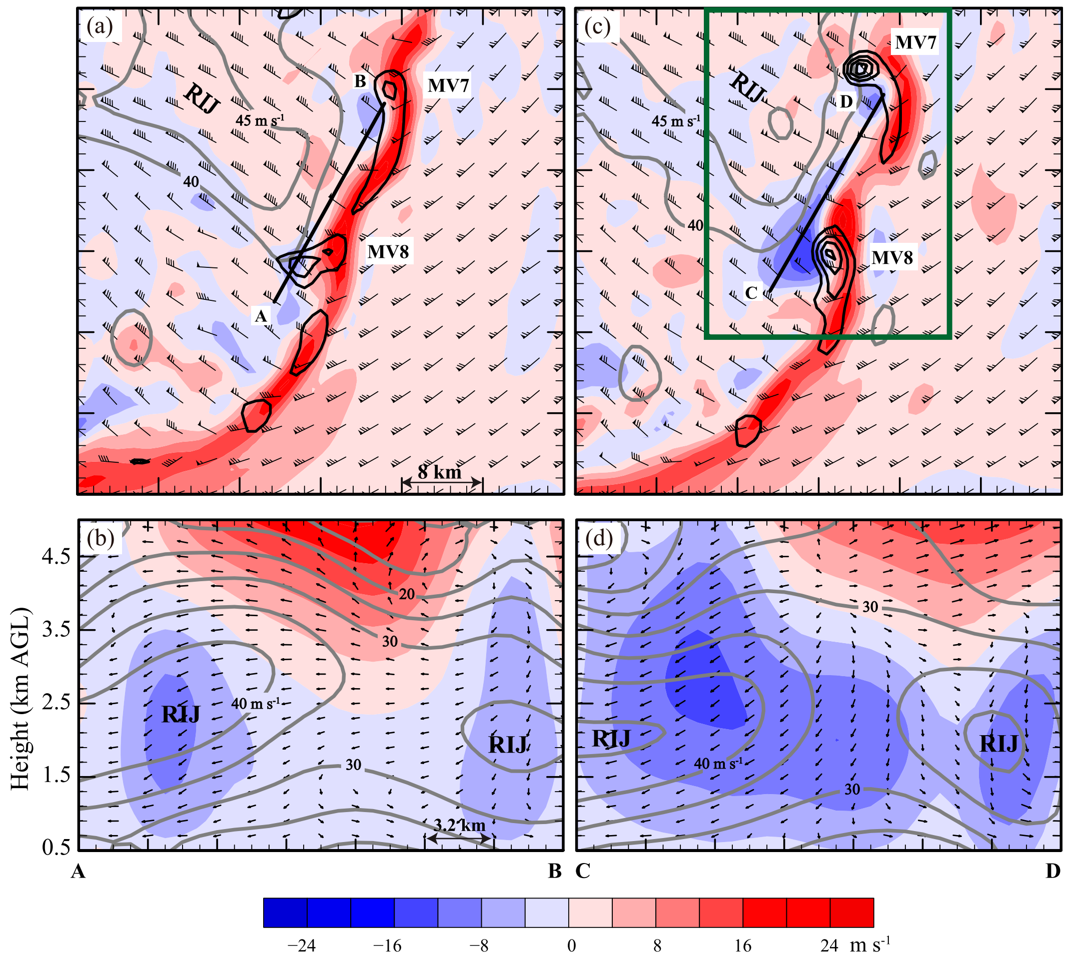

FIG. 19. Vertical velocity (shading), ground-relative wind field (vector), and speed (gray contour) on the horizontal plane of 3 km AGL at (a) 1440 and (c) 1445 UTC. (b),(d) As in (a),(c), but in the vertical plane through lines AB and CD shown in (a) and (c). The vertical vorticity at 200 m AGL (black contours, $\geq 0.005\ \mathrm{s}^{-1}$ at $0.005\ \mathrm{s}^{-1}$ interval) are also shown in (a) and (c). The green box in (c) indicates the domain shown in Fig. 20.

boundary conditions [see appendix A of Rotunno and Klemp (1985)]:

$$\nabla^2 p'_d = -\nabla \cdot (\overline{\rho}\mathbf{V} \cdot \nabla \mathbf{V}), \tag{3}$$

$$\nabla^2 p'_b = \frac{\partial \overline{\rho} b}{\partial z}, \tag{4}$$

where $\mathbf{V} = (u, v, w)$ is the 3D velocity vector. Once p'_d and p'_b are diagnosed, each term in the vertical momentum equation in (1) can be readily obtained, except for the mixing term, which is omitted here because it is relatively small.

The total vertical acceleration (Dw/Dt), dynamic vertical pressure gradient force (DVPGF), and effective buoyancy B on the horizontal plane at 3 km AGL are shown in Fig. 20. Figure 21 is similar to Fig. 20 but in the vertical plane through line CD (see Fig. 19c). Notable downward accelerations are found associated with the two strong downdrafts behind the leading-edge updrafts, whereas the downward accelerations between them are much weaker (Fig. 20a). The downward accelerations do not extend all the way to the surface because of necessary de-acceleration as the flow approaches the ground. In fact, positive vertical acceleration is found below about 1.5 km AGL (Fig. 21a).

The dynamically induced vertical pressure gradient force is found to be responsible for the downward accelerations of the two strong downdrafts above 2.5 km AGL, as well as for the broad deceleration of downdrafts at low levels (Fig. 21b). The dynamic forcing on the right-hand side of (3) has been separated into several parts that involve fluid extension and shear (Rotunno and Klemp 1985), or fluid strain and rotation (Trapp and Weisman 2003), to help understand the dynamics. Because it is the overall role of vertical dynamic pressure in the descent of the RIJ that we are most interested in,

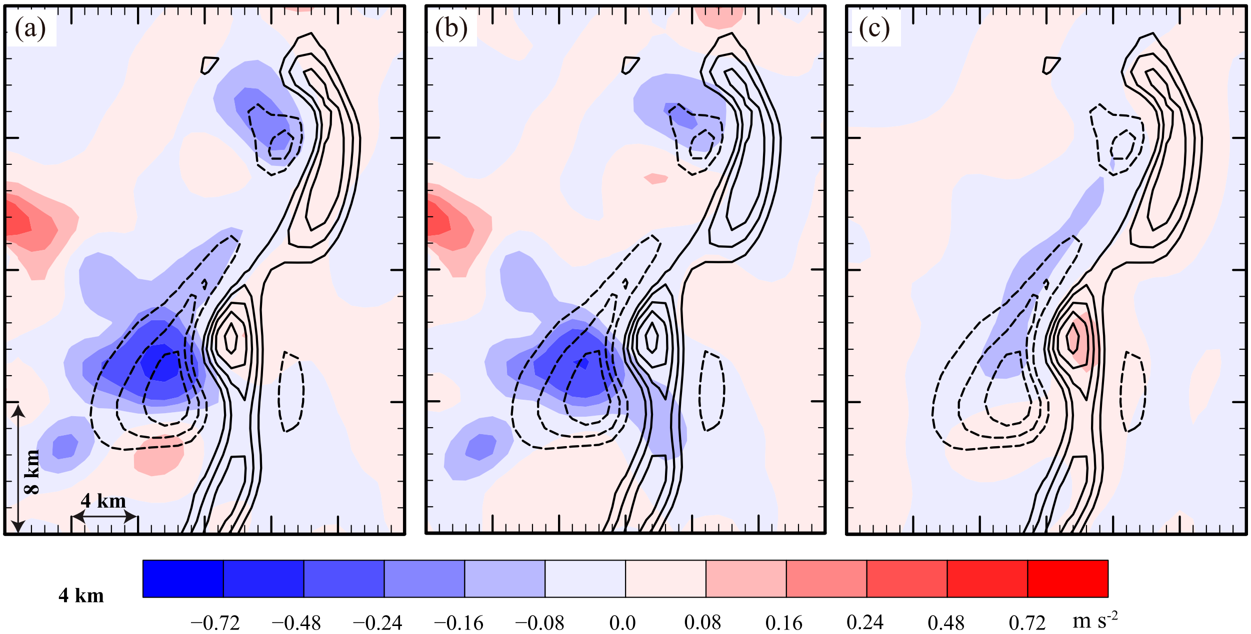

FIG. 20. (a) Total vertical velocity tendency, (b) dynamic vertical pressure gradient force, and (c) effective buoyancy at 3 km AGL at 1445 UTC. Black contours are for the vertical velocity at 3 km AGL, with negative values dashed. The positive and negative vertical velocities are contoured at values of 8, 12, 16, 20, and 24, and −4, −8, and $-12\,\mathrm{m\,s^{-1}}$, respectively. The plotted domain is 24 km by 32 km, as indicated by the green box in Fig. 19c.

more detailed diagnostics of the dynamic vertical pressure gradient force are not described herein. As for the buoyancy force, it is most negative at about 2 km AGL and it largely accounts for the weak downward acceleration between the two intense downdrafts (Fig. 21c). The buoyancy B can be further divided into contributions from precipitation loading [i.e., q_w term in (2)], and from thermal effects. From Fig. 22a, precipitation loading only generates negative buoyancy that is of fairly small spatial variation. Two strips of high (negative) buoyancy extend from aloft to the two strong downdrafts. On the contrary, temperature effects can create both negative and positive buoyancy (Fig. 22b). The negative buoyancy is most evident at 2 km AGL, which is likely attributed to evaporative cooling and/or melting of frozen hydrometeors there. For the positive buoyancy above 4 km and below 1 km AGL, the former one clearly occurs with the buoyant updrafts, while the latter one is due to the presence of the system cold pool in the low levels. Overall, the dynamic pressure gradient force dominates over the buoyancy term and is therefore the main driver of the locally enhanced descent of RIJ and the formation of strong surface winds near the mesovortex. Such strong surface winds create strong surface convergence that can promote formation of MVs through vertical stretching of vorticity (e.g., Trapp and Weisman 2003; Wheatley and Trapp 2008), which will be the focus of a companion paper. We point out here that the MV8 analyzed in detail in this section is the strongest and longest-lived MV found in our simulation. It is formed near the bow apex and is associated with the RIJ. An understanding of the evolution and characteristics of other weaker MVs in the simulation will require further analysis.

7. Summary and conclusions

This study presents an analysis of a derecho-producing bow echo and their embedded mesovortices (MVs) observed over the central United States on 8 May 2009, based on Doppler radar observations and a 800-m grid spacing, real-data model simulation using WRF. The bow echo developed in an environment of weak synoptic-scale forcing, but was fed by warm, moist air transported to the region by a strong low-level jet. Emphasis of this study is on documenting the existence, evolution, and characteristic of low-level MVs that form at the leading edge of the bow echo. The high winds produced near the surface, and their relationship with the bow-echo MVs, are also examined.

The observed MCS developed into a large bowing system from 1200 UTC 8 May 2009. Rotating reflectivity spirals developed on the northern portion of the system, with a hook-shaped echo forming at the northern end of the primary convective line. The overall system started to weaken around 1430 UTC while intense convection on the leading edge of the

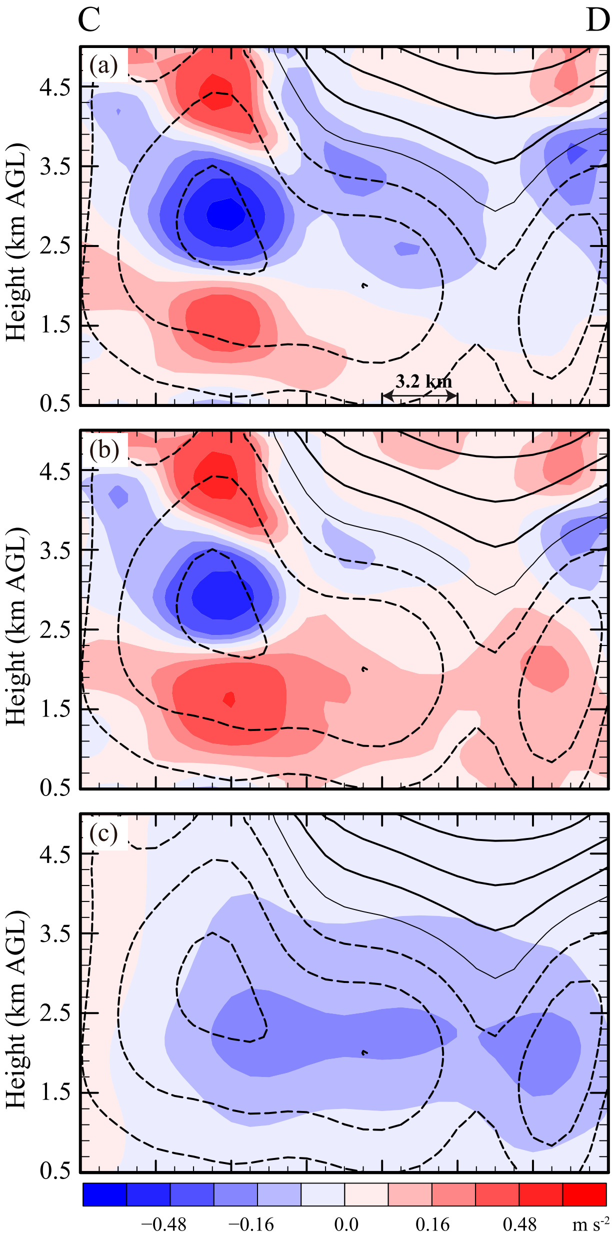

FIG. 21. (a) Total vertical velocity tendency, (b) dynamic vertical pressure gradient force, and (c) effective buoyancy in the vertical plane through line CD in Fig. 19c at 1445 UTC. Black contours are for the vertical velocity from −12 to 12 m s^{-1} at 4 m s^{-1} interval, with negative values dashed.

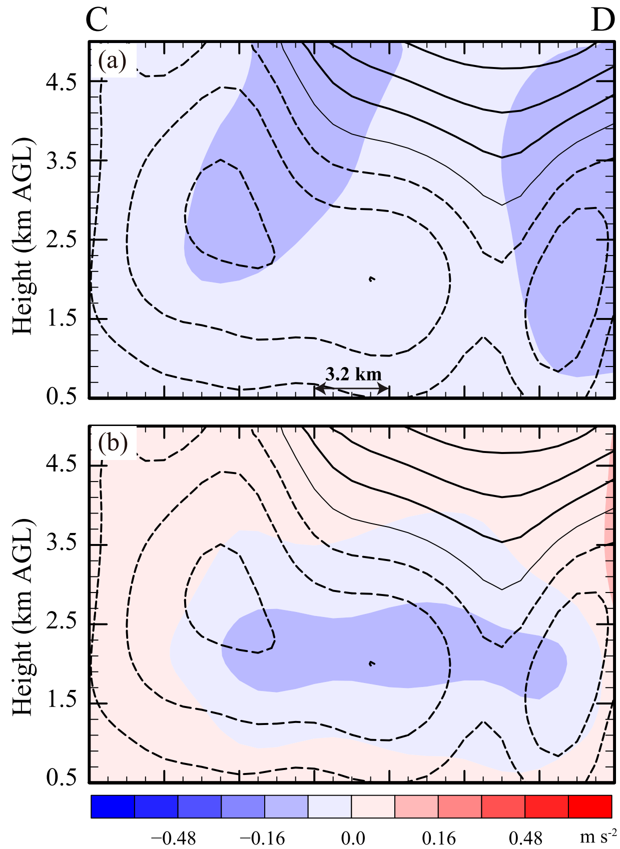

FIG. 22. (a) Effective buoyancy due to precipitation loading and (b) effective buoyancy excluding precipitation loading in the vertical plane through line CD in Fig. 19c at 1445 UTC. Black contours are for the vertical velocity from −12 to 12 m s^{-1} at 4 m s^{-1} interval, with negative values dashed.

system nearly vanished by 1530 UTC. Salient mesoscale features, including the RIJ behind the bow apex and the midlevel MCV over the northern portion of the bow echo are also clearly evident in the radar data. The WRF simulation at a 0.8-km grid spacing shows good agreement with the observed bow echo overall, although the observed reflectivity spirals and line-end hook are not as well developed in the simulation. There is also a nearly 2-h delay in the timing of simulated bow echo and the overall life is a little shorter. The general pattern and mesoscale features of the bow echo system are reproduced well, however.

A number of significant MVs are identified in the radar radial velocity data by using a linear least squares derivatives (LLSD) method, as well as in the WRF simulation databased on calculated vertical vorticity. These bow-echo MVs form on both sides of the bow apex but more predominantly on the northern half of the bow. The MVs developing on the southern part of the bow are in general weaker and shorter lived than their northern counterparts. Specifically, all reported tornadoes formed north of the bow apex. The MVs at (or near) the bow apex show consistent movement with the bow echo and persist for longer lifetime than those that are farther away from the apex. Mergers of like-signed vortices are often found as MVs move forward, which can lead to an upscale growth of MVs. Redevelopment is found for some MVs in the weakening stage of the system as a result of vortex mergers.

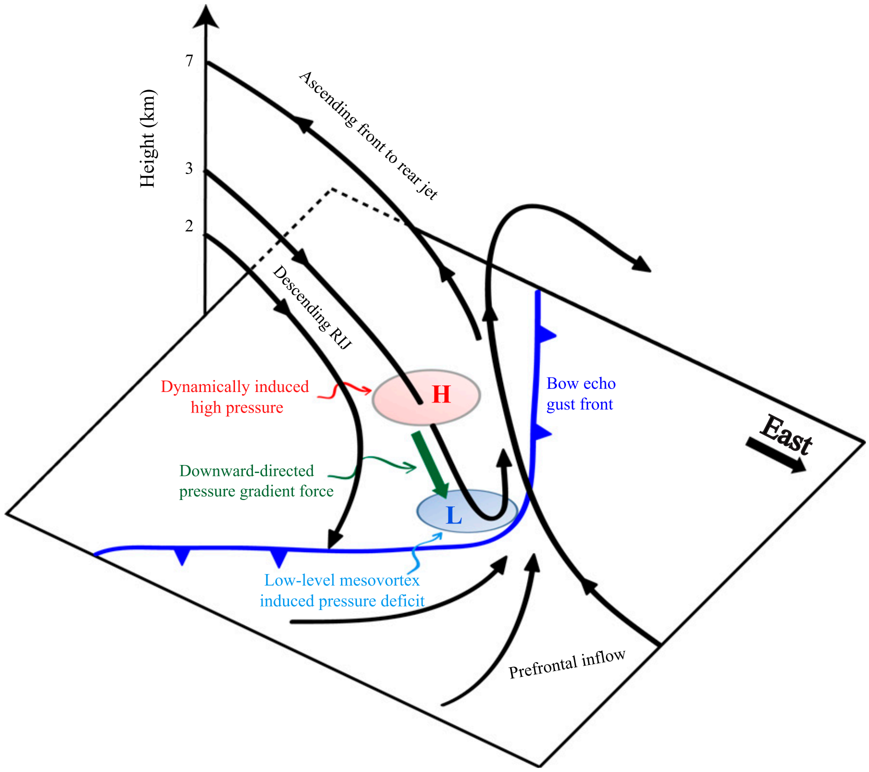

FIG. 23. Schematic of the descent of rear-inflow jet within a bow echo. The bow-echo gust front is marked in blue line with triangles. The prefrontal inflow, ascending front to rear jet, and descending rear-inflow jet (RIJ) are all depicted in black lines with arrows. As the rear-inflow jet impinges upon the convective updrafts at the bow-echo leading edge, it is blocked and creates a blocking high pressure (i.e., dynamically induced high pressure, pink ellipse marked with H). On the contrary, a low pressure is induced in the low level by the rotation of a leading-edge mesovortex (i.e., low-level mesovortex induced pressure deficit, azure ellipse marked with L). Consequently, a downward-directed pressure gradient force (dark green arrow) is generated that forces the descent of the rear-inflow jet.

Severe straight-line winds are also found near the surface within the simulation, mostly during the mature and decaying stages of the bowing system. The most damaging winds are found in association with a mesovortex (referred herein to as MV8) at the bow apex, which is embedded in the system RIJ. The presence of MV8 affects the positioning of the localized high-wind center. Kinematic removal of MV8 results in a northward displacement of the local wind speed maxima. Moreover, the vortical flow induced by MV8 accounts for a notable fraction of the high winds, MV8 therefore helps increase the severity of surface wind damage. The ambient flow owing to the descent of the RIJ is also shown to contribute significantly to the high winds near the ground. Analyses of the vertical velocity tendency reveal that it is in general the dynamically induced downward vertical pressure gradient force that causes the RIJ descent near the MV, as is schematically shown in Fig. 23 in a conceptual model. A blocking high pressure is created at the mid- to lower level as the RIJ impinges upon the convective updrafts at the bow-echo leading edge, while a low pressure is induced by the rotation of the low-level mesovortex. The resultant vertical pressure gradient force is thus directed downward, and acts to locally enhance the descent of the RIJ to the surface. Moreover, rapid increase is noted in the vertical vorticity of MV8 near the surface as the RIJ descends. As studied in a companion paper (Xu et al. 2015), this occurs as the descending RIJ enhances the low-level convergence and causes greater stretching of vertical vorticity. The strengthened low-level mesovortex in turn induces greater low pressure and, hence, a stronger downward pressure gradient force, which forces down the RIJ farther. However, the downward motion, especially that occurs within the vortex central column, is also a common cause for the filling and demise of low-level vortices, a process often referred to as the "vortex valve" effect (Lemon et al. 1975).

The results presented herein are one of the first of such kind, where a high-resolution (0.8-km grid spacing) real data simulation of a bow-echo system and embedded MVs are realistic enough to be directly comparable with radar measurements. We also performed Eulerian- and Lagrangian-based force analyses that show the dominant role of dynamic pressure gradient force over buoyancy as the main cause of the local enhancement of the RIJ descent near one of the MVs, which had not received systematic investigation before. Nevertheless, these conclusions are based on a single case and are not necessarily applicable to all bowing systems. Further studies on MVs and high winds for more bow-echo events are still needed, and this study represents one such effort in that direction.

Acknowledgments. This work was primarily supported by the National 973 Fundamental Research Program of China (2013CB430103), and by National Science Foundation of China Grants 40775034, 40575017, and 40830958. Xin Xu was supported by the Chinese Scholarship Council for his extended visit at the Center for Analysis and Prediction of Storms, University of Oklahoma. The third author acknowledges the support of the National Thousand Person Plan hosted at the Nanjing University, and the support of NSF Grants AGS-0802888, OCI-0905040, AGS-0941491, AGS-1046171, and AGS-1046081. Initial conversations with Dr. Michael Coniglio brought to our attention the mesovortices within this bow-echo case.

REFERENCES

Atkins, N. T., and M. St. Laurent, 2009a: Bow echo mesovortices. Part I: Processes that influence their damaging potential. *Mon. Wea. Rev.,* **137,** 1497–1513, doi:10.1175/2008MWR2649.1.

——, and ——, 2009b: Bow echo mesovortices. Part II: Their genesis. *Mon. Wea. Rev.,* **137,** 1514–1532, doi:10.1175/2008MWR2650.1.

——, J. M. Arnott, R. W. Przybylinski, R. A. Wolf, and B. D. Ketcham, 2004: Vortex structure and evolution within bow echoes. Part I: Single-Doppler and damage analysis of the 29 June 1998 derecho. *Mon. Wea. Rev.,* **132,** 2224–2242, doi:10.1175/1520-0493(2004)132<2224:VSAEWB>2.0.CO;2.

——, C. S. Bouchard, R. W. Przybylinski, R. J. Trapp, and G. Schmocker, 2005: Damaging surface wind mechanism within the 10 June 2003 Saint Louis bow echo during BAMEX. *Mon. Wea. Rev.,* **133,** 2275–2296, doi:10.1175/MWR2973.1.

Benjamin, S. G., and Coauthors, 2004: An hourly assimilation–forecast cycle: The RUC. *Mon. Wea. Rev.,* **132,** 495–518, doi:10.1175/1520-0493(2004)132<0495:AHACTR>2.0.CO;2.

Brewster, K., M. Hu, M. Xue, and J. Gao, 2005: Efficient assimilation of radar data at high resolution for short-range numerical weather prediction. *Extended Abstract, WWRP Int. Symp. Nowcasting Very Short Range Forecasting,* Toulouse, France, Météo-France, 3.06. [Available online at http://twister.ou.edu/papers/BrewsterWWRP_Nowcasting.pdf.]

Coniglio, M. C., S. F. Corfidi, and J. S. Kain, 2011: Environment and early evolution of the 8 May 2009 derecho-producing convective system. *Mon. Wea. Rev.,* **139,** 1083–1102, doi:10.1175/2010MWR3413.1.

——, ——, and ——, 2012: Views on applying RKW theory: An illustration using the 8 May 2009 derecho-producing convective system. *Mon. Wea. Rev.,* **140,** 1023–1043, doi:10.1175/MWR-D-11-00026.1.

Davis, C. A., and Coauthors, 2004: The Bow Echo and MCV Experiment (BAMEX): Observations and opportunities. *Bull. Amer. Meteor. Soc.,* **85,** 1075–1093, doi:10.1175/BAMS-85-8-1075.

Doswell, C. A., III, and P. M. Markowski, 2004: Is buoyancy a relative quantity? *Mon. Wea. Rev.,* **132,** 853–863, doi:10.1175/1520-0493(2004)132<0853:IBARQ>2.0.CO;2.

Ek, M. B., K. E. Mitchell, Y. Lin, E. Rogers, P. Grunmann, V. Koren, G. Gayno, and J. D. Tarpley, 2003: Implementation of Noah land surface model advances in the National Centers for Environmental Prediction operational mesoscale Eta model. *J. Geophys. Res.,* **108,** 8851, doi:10.1029/2002JD003296.

Evans, C., M. L. Weisman, and L. F. Bosart, 2014: Development of an intense, warm-core mesoscale vortex associated with the 8 May 2009 ''super derecho'' convective event. *J. Atmos. Sci.,* **71,** 1218–1240, doi:10.1175/JAS-D-13-0167.1.

Forbes, G. S., and R. M. Wakimoto, 1983: A concentrated outbreak of tornadoes, downbursts and microbursts, and implications regarding vortex classification. *Mon. Wea. Rev.,* **111,** 220–235, doi:10.1175/1520-0493(1983)111<0220:ACOOTD>2.0.CO;2.

Fujita, T. T., 1978: Manual of downburst identification for Project NIMROD. SMRP Paper 156, University of Chicago, 104 pp.

——, 1979: Objective, operation, and results of Project NIMROD. Preprints, *11th Conf. on Severe Local Storms,* Kansas City, MO, Amer. Meteor. Soc., 259–266.

Funk, T. W., K. E. Darmofal, J. D. Kirkpatrick, V. L. Dewald, R. W. Przybylinski, G. K. Schmocker, and Y.-J. Lin, 1999: Storm reflectivity and mesocyclone evolution associated with the 15 April 1994 squall line over Kentucky and southern Indiana. *Wea. Forecasting,* **14,** 976–993, doi:10.1175/1520-0434(1999)014<0976:SRAMEA>2.0.CO;2.

Grim, J. A., R. M. Rauber, G. M. McFarquhar, B. F. Jewett, and D. P. Jorgensen, 2009: Development and forcing of the rear inflow jet in a rapidly developing and decaying squall line during BAMEX. *Mon. Wea. Rev.,* **137,** 1206–1229, doi:10.1175/2008MWR2503.1.

Houze, R. A., Jr., M. I. Biggerstaff, S. A. Rutledge, and B. F. Smull, 1989: Interpretation of Doppler weather radar displays of midlatitude mesoscale convective systems. *Bull. Amer. Meteor. Soc.,* **70,** 608–619, doi:10.1175/1520-0477(1989)070<0608:IODWRD>2.0.CO;2.

Janjic, Z. I., 1994: The step-mountain eta coordinate model: Further developments of the convection, viscous sublayer, and turbulence closure schemes. *Mon. Wea. Rev.,* **122,** 927–945, doi:10.1175/1520-0493(1994)122<0927:TSMECM>2.0.CO;2.

Johns, R. H., and W. D. Hirt, 1987: Derechos: Widespread convectively induced windstorms. *Wea. Forecasting,* **2,** 32–49, doi:10.1175/1520-0434(1987)002<0032:DWCIW>2.0.CO;2.

Kong, F., and Coauthors, 2009: A real-time storm-scale ensemble forecast system: 2009 Spring Experiment. *23rd Conf. on Weather Analysis and Forecasting/19th Conf. on Numerical Weather Prediction,* Omaha, NE, Amer. Meteor. Soc., 16A.3.

[Available online at https://ams.confex.com/ams/23WAF19NWP/techprogram/paper_154118.htm.]

Lafore, J.-P., and M. W. Moncrieff, 1989: A numerical investigation of the organization and interaction of the convective and stratiform regions of tropical squall lines. *J. Atmos. Sci.,* **46,** 521–544, doi:10.1175/1520-0469(1989)046<0521:ANIOTO>2.0.CO;2.

Lemon, L. R., D. W. Burgess, and R. A. Brown, 1975: Tornado production and storm sustenance. Preprints, *Ninth Conf. Severe Local Storms,* Norman, OK, Amer. Meteor. Soc., 100–104.

Lese, A. D., and S. Martinaitis, 2010: Observations and quantification of counter-rotating mesovortex couplets within the 8 May 2009 southern Missouri derecho. *25th Conf. on Severe Local Storms,* Denver, CO, Amer. Meteor. Soc., 3B.3. [Available online at https://ams.confex.com/ams/25SLS/techprogram/paper_175427.htm.]

Mahoney, K. M., and G. M. Lackmann, 2011: The sensitivity of momentum transport and severe surface winds to environmental moisture in idealized simulations of a mesoscale convective system. *Mon. Wea. Rev.,* **139,** 1352–1369, doi:10.1175/2010MWR3468.1.

Meng, Z., F. Zhang, P. Markowski, D. Wu, and K. Zhao, 2012: A modeling study on the development of a bowing structure and associated rear inflow within a squall line over South China. *J. Atmos. Sci.,* **69,** 1182–1207, doi:10.1175/JAS-D-11-0121.1.

Newman, J. F., V. Lakshmanan, P. Heinselman, M. Richman, and T. Smith, 2013: Range-correcting azimuthal shear in Doppler radar data. *Wea. Forecasting,* **28,** 194–211, doi:10.1175/WAF-D-11-00154.1.

Orlanski, I., 1975: A rational subdivision of scales for atmospheric processes. *Bull. Amer. Meteor. Soc.,* **56,** 527–530.

Przybylinski, R. W., 1995: The bow echo: Observations, numerical simulations, and severe weather detection methods. *Wea. Forecasting,* **10,** 203–218, doi:10.1175/1520-0434(1995)010<0203:TBEONS>2.0.CO;2.

——, J. S. Schaumann, D. T. Cramer, and N. T. Atkins, 2010: The 08 May 2009 Missouri derecho: Radar analysis and warning implications over parts of southwest Missouri. *25th Conf. on Severe Local Storms,* Denver, CO, Amer. Meteor. Soc., 3B.1. [Available online at https://ams.confex.com/ams/25SLS/techprogram/paper_176095.htm.]

Rotunno, R., and J. B. Klemp, 1985: On the rotation and propagation of simulated supercell thunderstorms. *J. Atmos. Sci.,* **42,** 271–292, doi:10.1175/1520-0469(1985)042<0271:OTRAPO>2.0.CO;2.

——, ——, and M. L. Weisman, 1988: A theory for strong, long-lived squall lines. *J. Atmos. Sci.,* **45,** 463–485, doi:10.1175/1520-0469(1988)045<0463:ATFSLL>2.0.CO;2.

Schenkman, A. D., M. Xue, A. Shapiro, K. Brewster, and J. Gao, 2011: Impact of CASA radar and Oklahoma mesonet data assimilation on the analysis and prediction of tornadic mesovortices in an MCS. *Mon. Wea. Rev.,* **139,** 3422–3445, doi:10.1175/MWR-D-10-05051.1.

Skamarock, W. C., M. L. Weisman, and J. B. Klemp, 1994: Three-dimensional evolution of simulated long-lived squall lines. *J. Atmos. Sci.,* **51,** 2563–2584, doi:10.1175/1520-0469(1994)051<2563:TDEOSL>2.0.CO;2.

——, J. B. Klemp, J. Dudhia, D. O. Gill, D. M. Barker, W. Wang, and J. G. Powers, 2005: A description of the advanced research WRF version 2. NCAR Tech. Note NCAR/TN-468+STR, 88 pp. [Available online at http://www.mmm.ucar.edu/wrf/users/docs/arw_v2.pdf.]

Smith, T. M., and K. L. Elmore, 2004: The use of radial velocity derivatives to diagnose rotation and divergence. *11th Conf. on Aviation, Range and Aerospace,* Hyannis, MA, Amer. Meteor. Soc., P5.6. [https://ams.confex.com/ams/11aram22sls/techprogram/paper_81827.htm.]

Smull, B. F., and R. A. Houze Jr., 1987: Rear inflow in squall lines with trailing stratiform precipitation. *Mon. Wea. Rev.,* **115,** 2869–2889, doi:10.1175/1520-0493(1987)115<2869:RIISLW>2.0.CO;2.

Tao, W.-K., and Coauthors, 2003: Microphysics, radiation, and surface processes in the Goddard Cumulus Ensemble (GCE) model. *Meteor. Atmos. Phys.,* **82,** 97–137, doi:10.1007/s00703-001-0594-7.

Thompson, G., P. R. Field, R. M. Rasmussen, and W. D. Hall, 2008: Explicit forecasts of winter precipitation using an improved bulk microphysics scheme. Part II: Implementation of a new snow parameterization. *Mon. Wea. Rev.,* **136,** 5095–5115, doi:10.1175/2008MWR2387.1.

Trapp, R. J., and M. L. Weisman, 2003: Low-level mesovortices within squall lines and bow echoes. Part II: Their genesis and implications. *Mon. Wea. Rev.,* **131,** 2804–2823, doi:10.1175/1520-0493(2003)131<2804:LMWSLA>2.0.CO;2.

Wakimoto, R. M., H. V. Murphey, A. Nester, D. P. Jorgensen, and N. T. Atkins, 2006a: High winds generated by bow echoes. Part I: Overview of the Omaha bow echo 5 July 2003 storm during BAMEX. *Mon. Wea. Rev.,* **134,** 2793–2812, doi:10.1175/MWR3215.1.

——, ——, C. A. Davis, and N. T. Atkins, 2006b: High winds generated by bow echoes. Part II: The relationship between the mesovortices and damaging straight-line winds. *Mon. Wea. Rev.,* **134,** 2813–2829, doi:10.1175/MWR3216.1.

Weisman, M. L., 1992: The role of convectively generated rear-inflow jets in the evolution of long-lived mesoconvective systems. *J. Atmos. Sci.,* **49,** 1826–1847, doi:10.1175/1520-0469(1992)049<1826:TROCGR>2.0.CO;2.

——, 1993: The genesis of severe, long-lived bow echoes. *J. Atmos. Sci.,* **50,** 645–670, doi:10.1175/1520-0469(1993)050<0645:TGOSLL>2.0.CO;2.

——, and C. A. Davis, 1998: Mechanisms for the generation of mesoscale vortices within quasi-linear convective systems. *J. Atmos. Sci.,* **55,** 2603–2622, doi:10.1175/1520-0469(1998)055<2603:MFTGOM>2.0.CO;2.

——, and R. J. Trapp, 2003: Low-level mesovortices within squall lines and bow echoes. Part I: Overview and sensitivity to environmental vertical wind shear. *Mon. Wea. Rev.,* **131,** 2779–2803, doi:10.1175/1520-0493(2003)131<2779:LMWSLA>2.0.CO;2.

——, C. Evans, and L. Bosart, 2013: The 8 May 2009 superderecho: Analysis of a real-time explicit convective forecast. *Wea. Forecasting,* **28,** 863–892, doi:10.1175/WAF-D-12-00023.1.

Wheatley, D. M., and R. J. Trapp, 2008: The effect of mesoscale heterogeneity on the genesis and structure of mesovortices within quasi-linear convective systems. *Mon. Wea. Rev.,* **136,** 4220–4241, doi:10.1175/2008MWR2294.1.

——, ——, and N. T. Atkins, 2006: Radar and damage analysis of severe bow echoes observed during BAMEX. *Mon. Wea. Rev.,* **134,** 791–806, doi:10.1175/MWR3100.1.

Xu, X., M. Xue, and Y. Wang, 2015: The genesis of mesovortices within a real-data simulation of a bow echo system. *J. Atmos. Sci.,* doi:10.1175/JAS-D-14-0209.1, in press.

Xue, M., K. K. Droegemeier, and V. Wong, 2000: The Advanced Regional Prediction System (ARPS)—A multi-scale non-hydrostatic atmospheric simulation and prediction model. Part I: Model dynamics and verification. *Meteor. Atmos. Phys.,* **75,** 161–193, doi:10.1007/s007030070003.

——, D.-H. Wang, J.-D. Gao, K. Brewster, and K. K. Droegemeier, 2003: The Advanced Regional Prediction System (ARPS), storm-scale numerical weather prediction and data assimilation. *Meteor. Atmos. Phys.,* **82,** 139–170, doi:10.1007/s00703-001-0595-6.

——, and Coauthors, 2009: CAPS realtime 4-km multi-model convection-allowing ensemble and 1-km convection-resolving forecasts for the NOAA Hazardous Weather Testbed 2009 Spring Experiment. *23rd Conf. on Weather Analysis and Forecasting/19th Conf. on Numerical Weather Prediction,* Omaha, NE, Amer. Meteor. Soc., 16A.2.

Yang, M., and R. A. Houze Jr., 1995: Sensitivity of squall-line rear inflow to ice microphysics and environmental humidity. *Mon. Wea. Rev.,* **123,** 3175–3193, doi:10.1175/1520-0493(1995)123<3175:SOSLRI>2.0.CO;2.